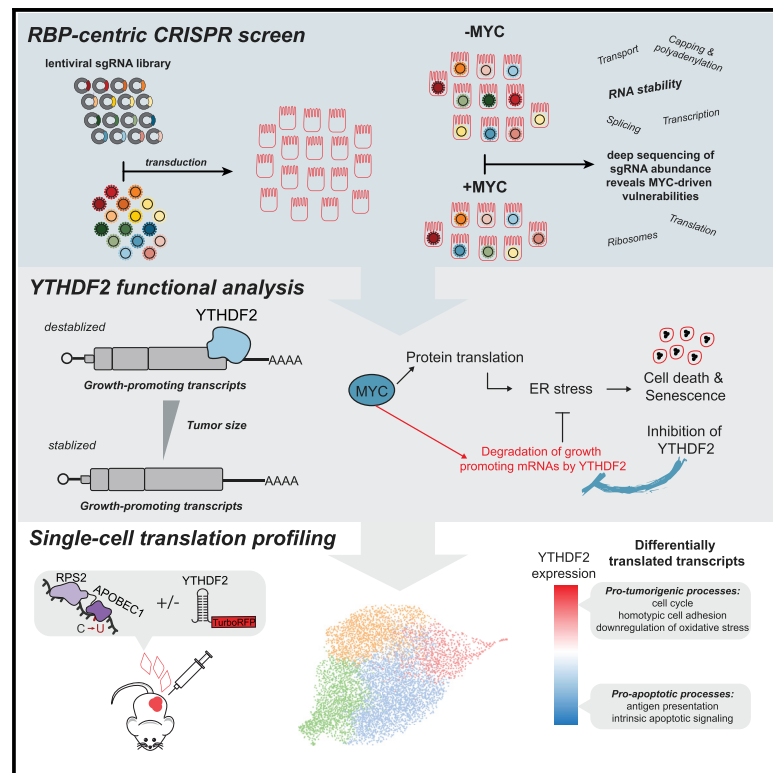


# Inhibition of YTHDF2 triggers proteotoxic cell death in MYC-driven breast cancer

## Graphical abstract



## Authors

Jaclyn M. Einstein, Mark Perelis, Isaac A. Chaim, ..., Siddhartha Tyagi, Thomas F. Westbrook, Gene W. Yeo

## Correspondence

geneyeo@ucsd.edu

## In brief

RNA-binding proteins (RBPs) are aberrantly expressed in cancer, but they remain largely unexplored as drug targets. Using RBP-focused CRISPR-Cas9 screening, Einstein et al. uncover an essential and selective role for YTHDF2 in MYC-driven breast cancer, highlighting the utility of discovering RBPs as safe and effective therapeutic targets.

## Highlights

- RBP CRISPR screening identifies 57 candidates that maintain MYC-driven cell survival
- YTHDF2 depletion triggers apoptosis in triple-negative breast cancer cells and tumors
- YTHDF2 maintains mRNA homeostasis by limiting the number of translating mRNAs
- scRibo-STAMP reveals proteomic heterogeneity in triple-negative breast tumors *in vivo*

Article

# Inhibition of YTHDF2 triggers proteotoxic cell death in MYC-driven breast cancer

Jaclyn M. Einstein,<sup>1,2,3</sup> Mark Perelis,<sup>1,2,3</sup> Isaac A. Chaim,<sup>1,2,3</sup> Jitendra K. Meena,<sup>4,5</sup> Julia K. Nussbacher,<sup>1,2,3</sup> Alexandra T. Tankka,<sup>1,2,3</sup> Brian A. Yee,<sup>1,2,3</sup> Heyuan Li,<sup>4,5</sup> Assael A. Madrigal,<sup>1,2,3</sup> Nicholas J. Neill,<sup>4,5</sup> Archana Shankar,<sup>1,2,3</sup> Siddhartha Tyagi,<sup>4,5</sup> Thomas F. Westbrook,<sup>4,5,6</sup> and Gene W. Yeo<sup>1,2,3,7,\*</sup>

<sup>1</sup>Department of Cellular and Molecular Medicine, University of California, San Diego, La Jolla, CA, USA

<sup>2</sup>Stem Cell Program, University of California, San Diego, La Jolla, CA, USA

<sup>3</sup>Institute for Genomic Medicine, University of California, San Diego, La Jolla, CA, USA

<sup>4</sup>Verna & Marrs McLean Department of Biochemistry and Molecular Biology, Baylor College of Medicine, Houston, TX 77030, USA

<sup>5</sup>Department of Molecular and Human Genetics, Baylor College of Medicine, Houston, TX 77030, USA

<sup>6</sup>Therapeutic Innovation Center (THINC), Baylor College of Medicine, Houston, TX 77030, USA

<sup>7</sup>Lead contact

\*Correspondence: [geneyeo@ucsd.edu](mailto:geneyeo@ucsd.edu)

<https://doi.org/10.1016/j.molcel.2021.06.014>

## SUMMARY

RNA-binding proteins (RBPs) are critical regulators of post-transcriptional gene expression, and aberrant RBP-RNA interactions can promote cancer progression. Here, we interrogate the function of RBPs in cancer using pooled CRISPR-Cas9 screening and identify 57 RBP candidates with distinct roles in supporting MYC-driven oncogenic pathways. We find that disrupting YTHDF2-dependent mRNA degradation triggers apoptosis in triple-negative breast cancer (TNBC) cells and tumors. eCLIP and m<sup>6</sup>A sequencing reveal that YTHDF2 interacts with mRNAs encoding proteins in the MAPK pathway that, when stabilized, induce epithelial-to-mesenchymal transition and increase global translation rates. scRibo-STAMP profiling of translating mRNAs reveals unique alterations in the translome of single cells within YTHDF2-depleted solid tumors, which selectively contribute to endoplasmic reticulum stress-induced apoptosis in TNBC cells. Thus, our work highlights the therapeutic potential of RBPs by uncovering a critical role for YTHDF2 in counteracting the global increase of mRNA synthesis in MYC-driven breast cancers.

## INTRODUCTION

Changes in cellular growth rate and identity that occur during cancer progression are driven by specific gene expression signatures programmed by the activity of DNA-binding transcription factors (TFs) and RNA-binding proteins (RBPs). To support high oncogenic growth rates, cancer cells generally require increased levels of transcription and global pre-RNA synthesis controlled by TFs, consequently increasing the cell's dependence on post-transcriptional processing by RBPs. Although TF mutations have been studied for decades, RBPs have been overlooked as drivers of disease and as therapeutically relevant targets. RBPs determine the fate of transcribed RNAs by regulating their splicing, polyadenylation, translation, subcellular localization, and turnover (Hentze et al., 2018). Somatic mutations, as well as epigenetic and post-translational modifications, can cause aberrant RBP expression in cancer cells, which can promote cell division, cell survival, metastasis, angiogenesis, and host immune evasion (Pereira et al., 2017). However, RBPs remain largely unexplored as drug targets because their systematic evaluation has been limited by the lack of sensitive and efficient

assays for phenotypic interrogation of individual RBPs (Pereira et al., 2017).

C-MYC (MYC) is the primary oncogenic driver of cancer gene expression programs in a broad spectrum of cancer types in which cells become “addicted” to and dependent on MYC for survival (Zuber et al., 2011). Although small molecules with the potential to inhibit MYC directly have recently emerged as clinical candidates (Han et al., 2019b; Struntz et al., 2019), they are likely to incur systemic toxic effects with long-term treatment, because of inhibition of MYC's physiological functions. Therefore, we used an orthogonal method by identifying RBPs that are selectively required to sustain MYC's oncogenic gene regulatory program using a synthetic lethality paradigm.

Here, we used human mammary epithelial cells (HMECs) expressing a MYC estrogen receptor (ER) fusion (MYC-ER HMECs) to test the hypothesis that the mutation of two genes (MYC and an RBP candidate) causes cell death, while the mutation of either gene individually is tolerated (Kessler et al., 2012). Using a CRISPR-Cas9 library targeting more than 1,000 RBPs in the human genome, we identified 57 RBPs that are required for the survival of MYC-hyperactive cells (Wheeler et al., 2020). Proteins known to mediate RNA catabolism were overrepresented

among RBP candidates, and we specifically found that depletion of YTHDF2 induced apoptosis in human triple-negative breast cancer (TNBC) cell lines and impeded xenografted tumor growth *in vivo*. Integrated analyses identified a role for YTHDF2 in the turnover of RNAs that contribute to epithelial-to-mesenchymal transition (EMT) initiation and tumorigenesis to limit the endoplasmic reticulum stress response that accompanies this process. Altogether, our study clarifies the molecular mechanisms underlying m<sup>6</sup>A-mediated gene regulation in MYC-driven breast cancer and highlights YTHDF2 as a safe and effective therapeutic target.

## RESULTS

### Identification of critical RBPs in MYC-driven breast cancer

To screen for RBP dependencies in cancer, we used a CRISPR-Cas9 lentiviral library containing 10 single-guide RNAs (sgRNAs) for each of 1,078 RBPs, 628 sgRNAs targeting essential genes as positive controls, and 1,058 non-targeting sgRNAs as negative controls (Wheeler et al., 2020). The small library size and specific focus on RBPs provides higher confidence hits and therefore higher reproducibility than whole-genome approaches typically using more shallow coverage of 3 or 4 sgRNAs per gene (Shalem et al., 2014). High-throughput sequencing confirmed that the plasmid library maintained sgRNA coverage and that aliquots were tightly correlated (less than 0.065% of sgRNAs received undetectable normalized read counts; Figure S1A).

We transduced MYC-ER HMECs with the CRISPR library in biological duplicate, selected for transduced cells with puromycin, treated half of the cells with tamoxifen (TAM) to induce MYC activity, and isolated genomic DNA (gDNA) 8 and 16 days after puromycin removal (Figure 1A). The representation of randomly integrated sgRNAs was tightly correlated with their frequencies in the original plasmid library, and replicate libraries were highly correlated (Figures S1B and S1C). We observed a significant reduction in sgRNA diversity in surviving cells on days 8 and 16 in both MYC-induced and uninduced HMECs, indicating dropout of cells transduced with sgRNAs targeting essential genes (positive controls) compared with cells transduced with non-targeting sgRNAs (negative controls) (Figures 1B, S1D, and S1E).

sgRNAs targeting 57 RBP candidates ( $p < 0.05$ ) were depleted in MYC-induced cell populations compared with uninduced control cells (Figure 1C; Table S1). Our analysis revealed RBPs that have been implicated in gene regulation downstream of MYC, including *PTBP1* (He et al., 2014), *PCBP2* (Wan et al., 2016), *ELAVL1* (Lafon et al., 1998), and *TRA2B* (Park et al., 2019) and identified ~40 RBPs previously unknown in this context. We observed enrichment for genes that negatively regulate macromolecule assembly, including several genes that repress exon inclusion (*HNRNPA2B1*, *PTBP1*, *SRSF9*), repress transcription (*ZGPAT*, *SLTM*), promote mRNA turnover (*YTHDF2*, *UPF3B*, *UPF3A*, *XRN1*, *DCP2*, *AGO2*), and prevent translation initiation (*EIF4ENIF1*, *EIF4E2*) (Figure 1C). This suggests vulnerabilities in MYC-hyperactive cells by RBPs that reduce the stability of mRNAs for translation, or RBPs that reduce protein translation rates.

We next cross-referenced public data from The Cancer Genome Atlas (TCGA) pan-cancer clinical data resource (Liu et al., 2018) and found that 67% of our RBP candidates are highly expressed in typically MYC-amplified basal-like TNBC tumors, compared with luminal A/luminal B, hormone receptor positive (HR+; estrogen receptor [ER] positive, progesterone receptor [PR] positive) or human epidermal growth factor receptor 2 positive (HER2+) breast tumors (Green et al., 2016; Figure 1D). Together, our results indicate that several RBPs controlling various stages of the RNA life cycle are aberrantly expressed in TNBC. As MYC-amplified cells typically contain increased quantities of mRNA, caused in part by 3' untranslated region (UTR) shortening (Mayr and Bartel, 2009), we further examined RBP candidates that regulate RNA stability and turnover. We found that the overall survival of patients with TNBC tumors containing above median MYC expression levels was significantly improved when tumors contained below median expression levels of mRNA decay factors *AGO2*, *EXOSC7*, *FUS*, *YTHDF2*, and *ZFP36L2* (Figure S1F).

### Depleting YTHDF2 induces apoptosis of TNBC tumors *in vivo*

Consistent with previous studies implicating aberrant mRNA methylation (Lan et al., 2019) and expression of m<sup>6</sup>A methyltransferases, demethylases, and m<sup>6</sup>A binding proteins in various cancers (Huang et al., 2018), we found that the m<sup>6</sup>A reader protein YTHDF2 is significantly upregulated in TNBC compared with HR+ and HER2+ breast cancers (Figure 1E). YTHDF2 mediates mRNA turnover by recruiting the CCR4-NOT deadenylase complex to initiate deadenylation and decay of m<sup>6</sup>A-containing transcripts before localizing with bound targets to processing (P) bodies for committed degradation (Du et al., 2016; Wang et al., 2014). However, the role of YTHDF2-mediated turnover of methylated RNA in cancer is not clear because of conflicting findings regarding its function (Paris et al., 2019; Zhong et al., 2019). Moreover, the direct and functionally relevant YTHDF2 target RNAs have yet to be defined in the mammary epithelium or in human breast cancer.

We first verified that loss of *YTHDF2* expression causes cell death in MYC-induced HMECs using two independent short hairpin RNA (shRNA)-mediated knockdowns of YTHDF2 (shYTHDF2-1 and shYTHDF2-2) (Figures 1F and S1G). After 24 h of MYC induction, we observed a significant increase in apoptotic, Annexin V-positive cells and early cell death in MYC-induced HMECs compared with uninduced controls (Figures 1G, 1H, and S1H). We also confirmed epistasis between YTHDF2 and m<sup>6</sup>A-modified RNA targets using shRNA-mediated knockdown of m<sup>6</sup>A writer, METTL3 (shMETTL3) (Figure 1F), which similarly triggered apoptotic cell death (Figures 1G, 1H, and S1H). In addition, using propidium iodide (PI) staining, we found that after 3 days of MYC induction, significantly more YTHDF2-depleted HMECs were assigned to sub-G1 cell cycle phase, and significantly fewer were assigned to G0/G1 phase, suggesting G1 checkpoint arrest. Uninduced HMECs did not show significant changes in fractions of cells assigned to G0/G1, S, or G2/M phases following YTHDF2 depletion (Figure 1I; Figure S1I). We also found that proliferation rates of TNBC cell lines (MDA-MB-231 and secondary lung metastatic MDA-MB-231-LM2) were

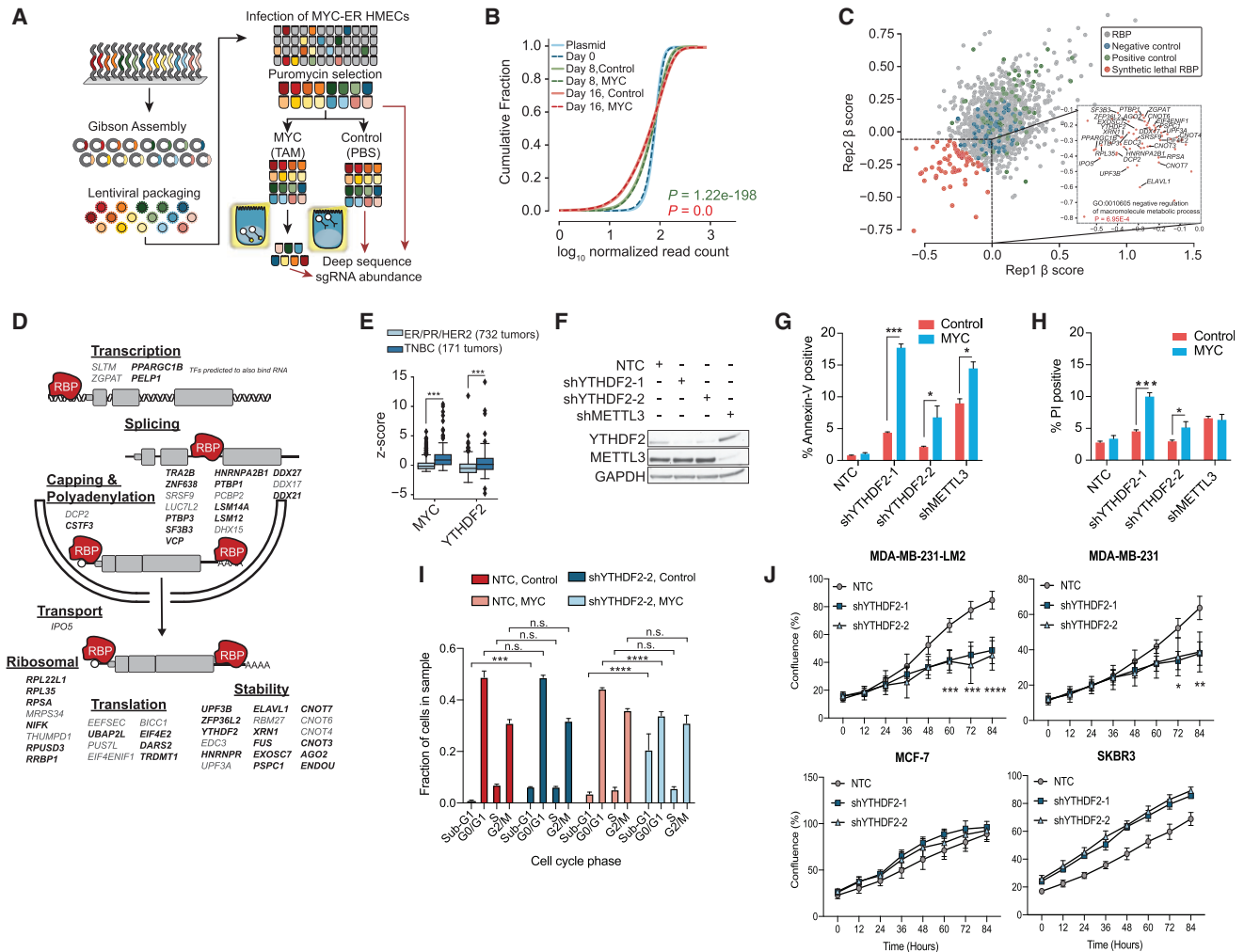


**Figure 1. RBP CRISPR screen identifies mRNA decay as a vulnerability in MYC-driven cancer**

(A) Schematic describing the generation and implementation of the RBP-targeted CRISPR screen in MYC-ER HMECs.  
 (B) Cumulative distribution of normalized read counts for sgRNAs in each sample. Each condition is representative of two independent replicates. Two-sided Kolmogorov-Smirnov tests compared with day 0.  
 (C) Comparison of  $\beta$  score replicates on day 16. Inset highlights synthetic lethal candidate RBPs, and genes enriched for “negative regulation of macromolecule metabolic process” are labeled.  
 (D) Schematic describing the function of RBP candidates identified in (C). RBPs in bold are significantly upregulated in basal-like TNBC tumors compared with ER/PR/HER2-positive tumors from TCGA data portal (Liu et al., 2018).  $p < 0.05$ , two-sided Student’s t test.  
 (E) Boxplot comparing mRNA expression levels for MYC and YTHDF2 between TNBC and ER/PR/HER2-positive tumors from TCGA data portal (Liu et al., 2018).  $***p < 0.001$ , two-sided Student’s t test.  
 (F) Western blot confirming shRNA-mediated knockdown in MYC-ER HMECs.  
 (G) Quantification of Annexin V staining in MYC-ER HMECs with indicated knockdowns with (blue) and without (red) 24 h of MYC induction.  $*p < 0.05$  and  $***p < 0.001$ , two-tailed Student’s t test. Bars are mean  $\pm$  SD;  $n = 3$  independent replicates.  
 (H) Quantification of propidium iodide (PI) staining in MYC-ER HMECs with indicated knockdowns with (blue) and without (red) 24 h of MYC induction.  $*p < 0.05$  and  $***p < 0.001$ , two-tailed Student’s t test. Bars are mean  $\pm$  SD;  $n = 3$  independent replicates.  
 (I) Quantification of cell cycle phase using PI in MYC-ER HMECs with indicated knockdowns with and without 3 days of MYC induction.  $***p < 0.001$  and  $****p < 0.0001$ , two-way ANOVA with Dunnett’s post hoc test for multiple comparisons. Bars are mean  $\pm$  SD;  $n = 3$  independent replicates.  
 (J) Cell proliferation of shYTHDF2 cells compared with non-targeting control (NTC) over time in TNBC, HR+, and HER2+ breast cancer cell lines.  $*p < 0.05$ ,  $**p < 0.01$ ,  $***p < 0.001$ , and  $****p < 0.0001$ , two-way ANOVA with Dunnett’s post hoc test for multiple comparisons. Values normalized to initial average confluence. Bars are mean  $\pm$  SD;  $n = 6$  independent replicates.

See also Figure S1.

significantly reduced following YTHDF2 depletion, while HR+ and HER2+ breast cancer cell lines (MCF-7 and SKBR3, respectively) were not (Figures 1J and S1J).

To determine the importance of genes encoding regulators of mRNA turnover on MYC-driven tumor growth *in vivo*, we generated a pool of MDA-MB-231-LM2 cells transduced with various doxycycline (DOX)-inducible, TurboRFP-tagged shRNAs targeting several proteins mediating RNA stability, three of which target YTHDF2, and assessed dropout of shRNAs both *in vitro* cultured cells and *in vivo* by subcutaneous mouse xenograft (Figure 2A; Table S2). We identified a YTHDF2-targeting hairpin that was significantly depleted in resected tumors and in cells cultured *in vitro* ( $p < 0.001$ ), indicating a growth disadvantage in TNBC cells upon silencing of YTHDF2 (Figures 2B–2D). To verify that YTHDF2 inhibition negatively affects tumor growth *in vivo*, we generated stable MDA-MB-231-LM2 cells transduced with the DOX-inducible shRNA identified by the screen (Figures S2A and S2B). Following DOX treatment, we confirmed that cells expressing the highest levels of the YTHDF2-targeting shRNA became depleted over time when cultured *in vitro*, suggesting death of cells with sufficient YTHDF2 depletion (Figure S2C). After initial tumor engraftment, we observed reduced growth rates and significantly smaller final tumor volumes from DOX-treated mice compared with tumors from vehicle-treated mice (Figures 2E–2G). In addition to fewer proliferating cells, we observed increased caspase-3 cleavage and a reduction in host angiogenic vascular endothelial cell markers in tumors from DOX-treated mice (Figures 2H, 2I, and S2D).

Next, we generated inducible multi-tissue *CAG-CreERT*; *Ythdf2*<sup>fl/fl</sup> mice by crossing *CAG-CreERT* mice with previously generated *Ythdf2*<sup>fl/fl</sup> mice (Li et al., 2018; Figure S2E) to expose any effects on the viability of healthy cells in other organs. Systemic genetic depletion of *Ythdf2* resulted in no gross physiological abnormalities or changes in body weight for at least 4 weeks following TAM administration (Figures S2F and S2G), nor did it induce programmed cell death in female reproductive tissues known to rely on m<sup>6</sup>A regulation by YTHDF2 (Ivanova et al., 2017; Figure S2H). This suggests that inhibition of *Ythdf2* in an intact organism has no adverse effects in non-cancerous somatic tissues and that YTHDF2 depletion safely and specifically inhibits growth of cells predisposed to MYC addiction.

### YTHDF2 targets are enriched for genes regulating growth factor signaling

To identify transcript-specific functions of YTHDF2 targets in MYC-driven cancer, we performed enhanced crosslinking and immunoprecipitation (eCLIP) (Van Nostrand et al., 2017) and m<sup>6</sup>A sequencing (m<sup>6</sup>A-seq) (Dominissini et al., 2013) in MYC-induced and uninduced HMECs, MDA-MB-231-LM2 cells, MDA-MB-231 cells, MCF-7 cells, and SKBR3 cells in biological duplicate (Figure S3A; Table S3). In agreement with previous YTHDF2 CLIP and RNA immunoprecipitation (RIP) sequencing experiments, we found that a majority of high-confidence YTHDF2 and m<sup>6</sup>A peaks map to the 3' end of transcripts in the coding sequence (CDS) and 3' UTR (Figure 3A) and contain the DRACH (D = A, G, or U; R = A or G; H = A, C, or U) sequence motif (Figure 3B). We confirmed that YTHDF2 binding sites generally overlap with m<sup>6</sup>A-modified sites using pairwise comparisons be-

tween eCLIP and m<sup>6</sup>A-seq IP reads at each m<sup>6</sup>A site and that eCLIP IP reads were enriched at m<sup>6</sup>A sites over size-matched (SM) inputs (Figures S3B and S3C). Collectively, our epitrancriptomic analyses confirm binding of YTHDF2 at m<sup>6</sup>A-modified sites on RNAs containing the consensus sequence.

To determine if MYC activity influences the m<sup>6</sup>A landscape, we compared high-confidence m<sup>6</sup>A sites among MYC-induced and uninduced HMECs and among TNBC, HR+, and HER2+ breast cancer cell lines. Interestingly, we found that the secondary lung metastatic MDA-MB-231-LM2 tumor cells appeared to acquire new m<sup>6</sup>A modifications, as ~72% of m<sup>6</sup>A sites (14,873 peaks) and ~46% modified genes (4,512 genes) were unique from the parental MDA-MB-231 cell line (Figure 3C). Consistent with previous studies (Lin et al., 2016), this suggests that the m<sup>6</sup>A landscape is modified during tumor evolution and metastasis, indicating that cancer cells become increasingly reliant on m<sup>6</sup>A-dependent RNA regulation as they become more invasive. However, MYC-induced HMECs did not display robust differences in m<sup>6</sup>A-modified sites compared with uninduced HMECs in either direction, and neither did HR+ or HER2+ breast cancer cell lines compared with MDA-MB-231 cells, suggesting that MYC activity does not determine the m<sup>6</sup>A landscape in mammary tumors (Figure 3C).

As RBP binding affinity is driven largely by RNA sequence and secondary structure, which are conserved across cell types and states (Lambert et al., 2014), we expect that differences in YTHDF2 binding targets among cancer cell lines result from differences in target RNA expression level and alterations in m<sup>6</sup>A status. To understand YTHDF2's role in promoting MYC-driven cancer cell growth and survival and to pinpoint the targets that uniquely contribute to apoptosis, we analyzed RNA expression data for overlapping YTHDF2 targets in TNBC cell lines (Figure 3D). Using hierarchical clustering of Z scores, we identified two clusters (red and blue) in which YTHDF2 targets are highly expressed in TNBC cells compared with HR+ and HER2+ cells (Figure 3E). These clusters were enriched for genes that regulate wound healing, cell adhesion, ERK1/2 signaling, and EMT, while clusters including genes that are also highly expressed in MCF-7 cells (yellow and green) generally lack enrichment for genes belonging to these ontology terms (Figure 3F).

### Depletion of YTHDF2 upregulates EMT-specific pathways

We next verified that TNBC cells undergo expression changes resembling EMT following YTHDF2 depletion by performing RNA sequencing (RNA-seq) in YTHDF2-depleted, MYC-induced HMECs in biological duplicate. We found that transcripts that are bound by YTHDF2 are upregulated compared with transcripts lacking binding sites (Figure 4A), but inspection of the individual upregulated mRNAs revealed that >50% of upregulated transcripts were not direct YTHDF2 targets. These include *CPA4*, *HMOX1*, and *MMP3*, which are known to contribute to or are transcribed in response to cell migration, wound healing, and metastatic phenotypes (Handa et al., 2019; Zhu et al., 2017, 2019; Figure 4B). These genes exhibited very low or undetectable RNA expression (transcripts per million [TPM] ≤ 1) in non-targeting control (NTC) cells yet were dramatically increased (~30–85 TPM) in YTHDF2-depleted cells. Among expressed genes, 4.8% (Bonferroni-adjusted  $p$  [padj] < 0.001, log<sub>2</sub> fold

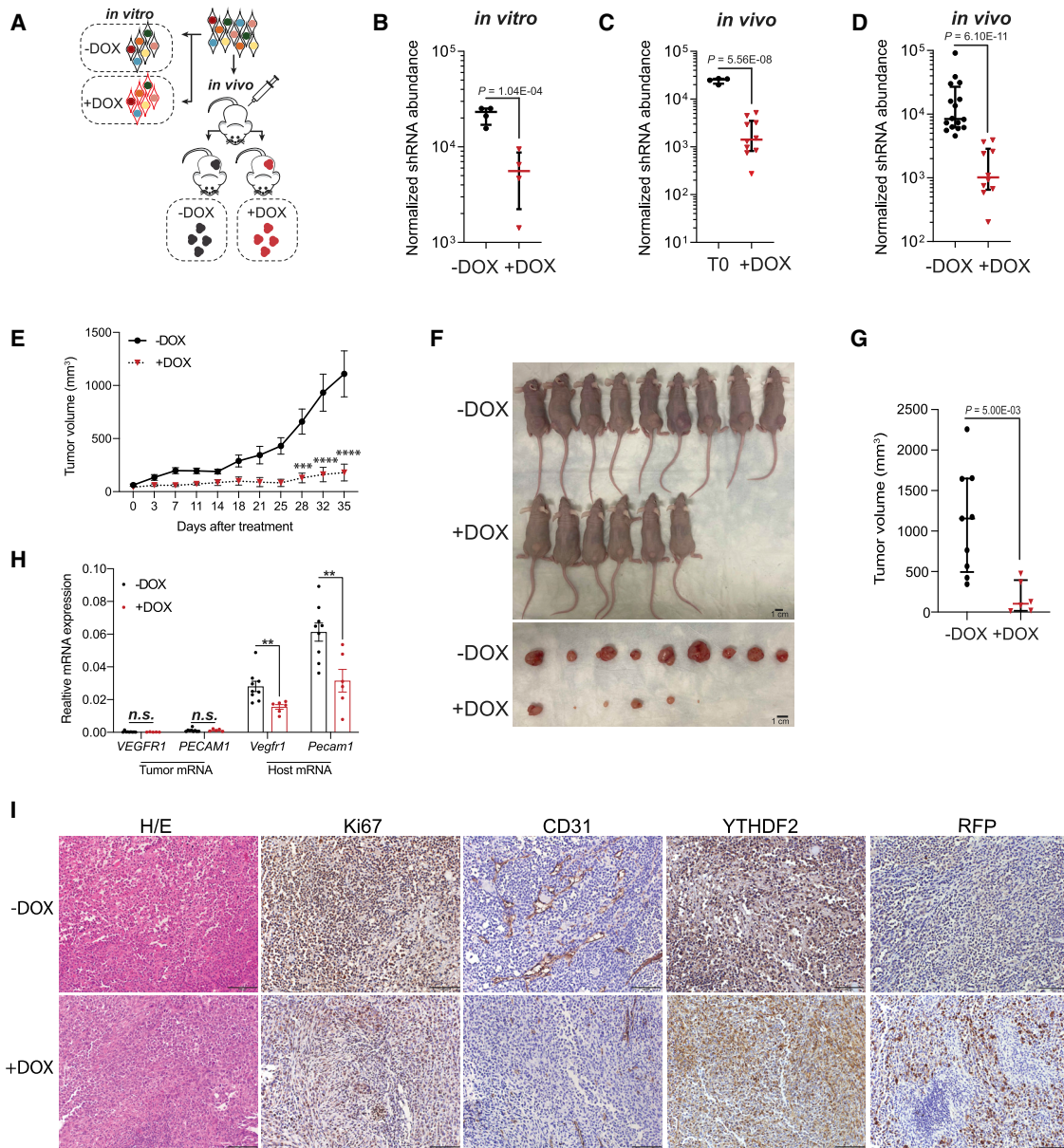


**Figure 2. Depletion of YTHDF2 in TNBC cells suppresses tumor growth *in vivo***

(A) Schematic of pooled shRNA screen conducted in MDA-MB-231-LM2 cells *in vitro* and *in vivo*.

(B–D) Dot plots quantifying shRNA normalized abundance following doxycycline (DOX)-induced knockdown of MDA-MB-231-LM2 cells (B) *in vitro* ( $n = 4$  independent replicates) and (C and D) *in vivo*. Dots represent individual tumor samples. Bars are median  $\pm$  quartile. T0 is the tumor composition when DOX was introduced. –DOX,  $n = 16$  mice; +DOX,  $n = 10$  mice.

(E) Average tumor volume over time of DOX-induced, YTHDF2-depleted xenografted mice compared with vehicle controls. \*\*\* $p < 0.001$  and \*\*\*\* $p < 0.0001$ , two-way ANOVA with Dunnett’s post hoc test for multiple comparisons. Bars are mean  $\pm$  SEM; –DOX,  $n = 9$  mice; +DOX,  $n = 6$  mice.

(F) Images of mice 35 days following DOX induction compared with vehicle controls. Scale bars, 1 cm.

(G) Tumor volumes 35 days following DOX induction compared with vehicle controls. –DOX,  $n = 9$  mice; +DOX,  $n = 6$  mice.  $p$  values calculated using two-sided Student’s  $t$  test.

(H) qRT-PCR analysis relative to *Gapdh* of mRNA extracted from final tumors, 35 days following DOX induction. \*\* $p < 0.01$ ; n.s., not significant, two-sided Student’s  $t$  test. Bars are mean  $\pm$  SEM; –DOX,  $n = 9$  vehicle mice; +DOX,  $n = 6$  mice.

(I) Immunohistochemical staining of DOX-treated and vehicle control tumor sections, 35 days following DOX induction. Scale bars, 100  $\mu$ m.

See also [Figure S2](#).

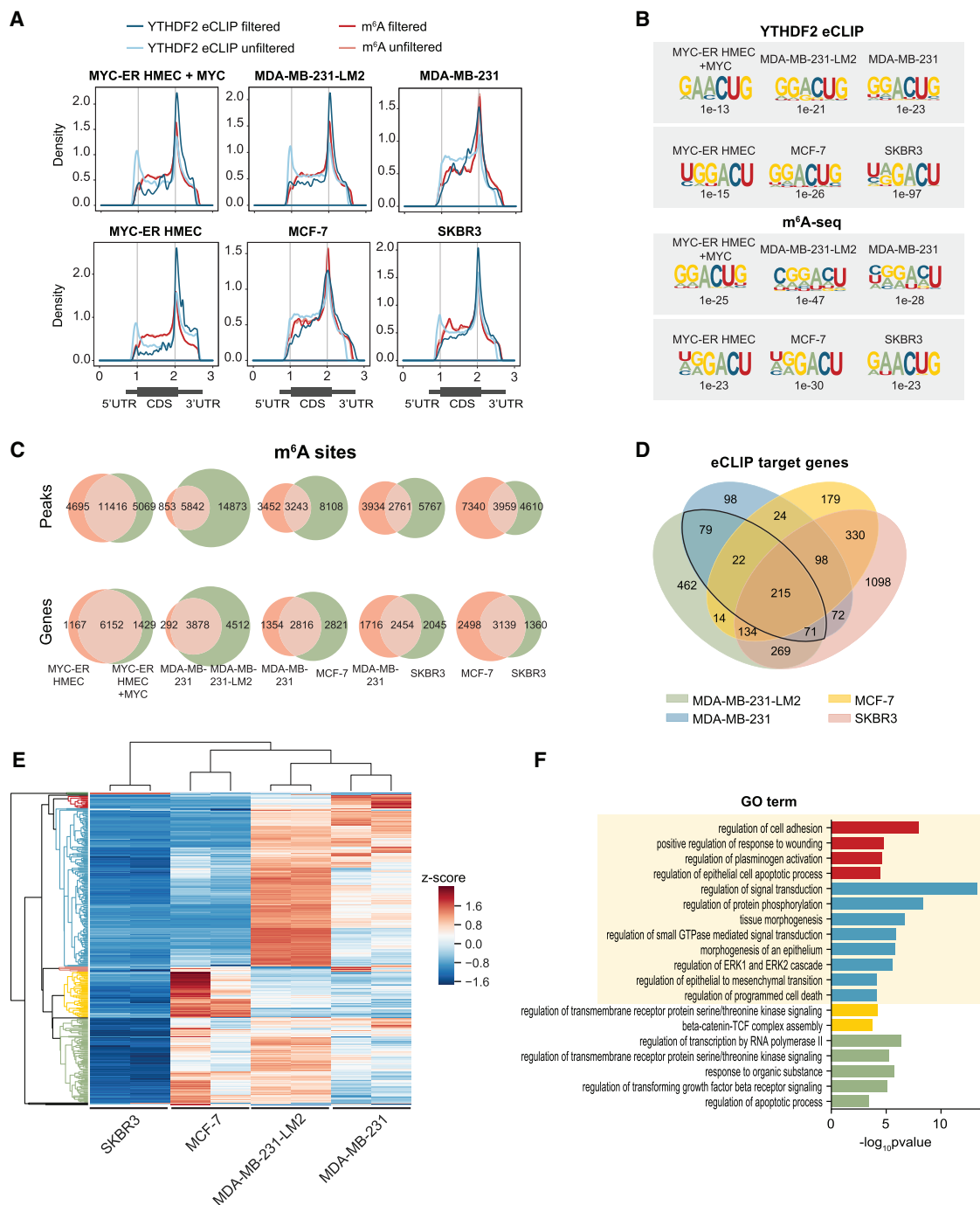


**Figure 3. eCLIP and m<sup>6</sup>A-seq identify MAPK/ERK pathway transcripts that are regulated by YTHDF2**

(A) Metagenes profiles of filtered and unfiltered eCLIP (blue) and m<sup>6</sup>A-seq (red) peak enrichment.

(B) Motif analysis of unfiltered eCLIP (top) and m<sup>6</sup>A-seq (bottom) data. Representative of two independent replicates.

(C) Venn diagram overlaps of high-confidence m<sup>6</sup>A-seq peak and gene enrichment.

(D) Four-way Venn diagram of overlapping, high-confidence YTHDF2 target genes among TNBC, HR+, and HER2+ breast cancer cell lines. Genes overlapping in TNBC cell lines are outlined.

(E) Hierarchical cluster map illustrating expression levels of overlapping YTHDF2 target genes outlined in (D). Gene clusters are depicted in the dendrogram.

(F) Gene Ontology (GO) enrichment of genes in dendrogram clusters from (E).

See also Figure S3.

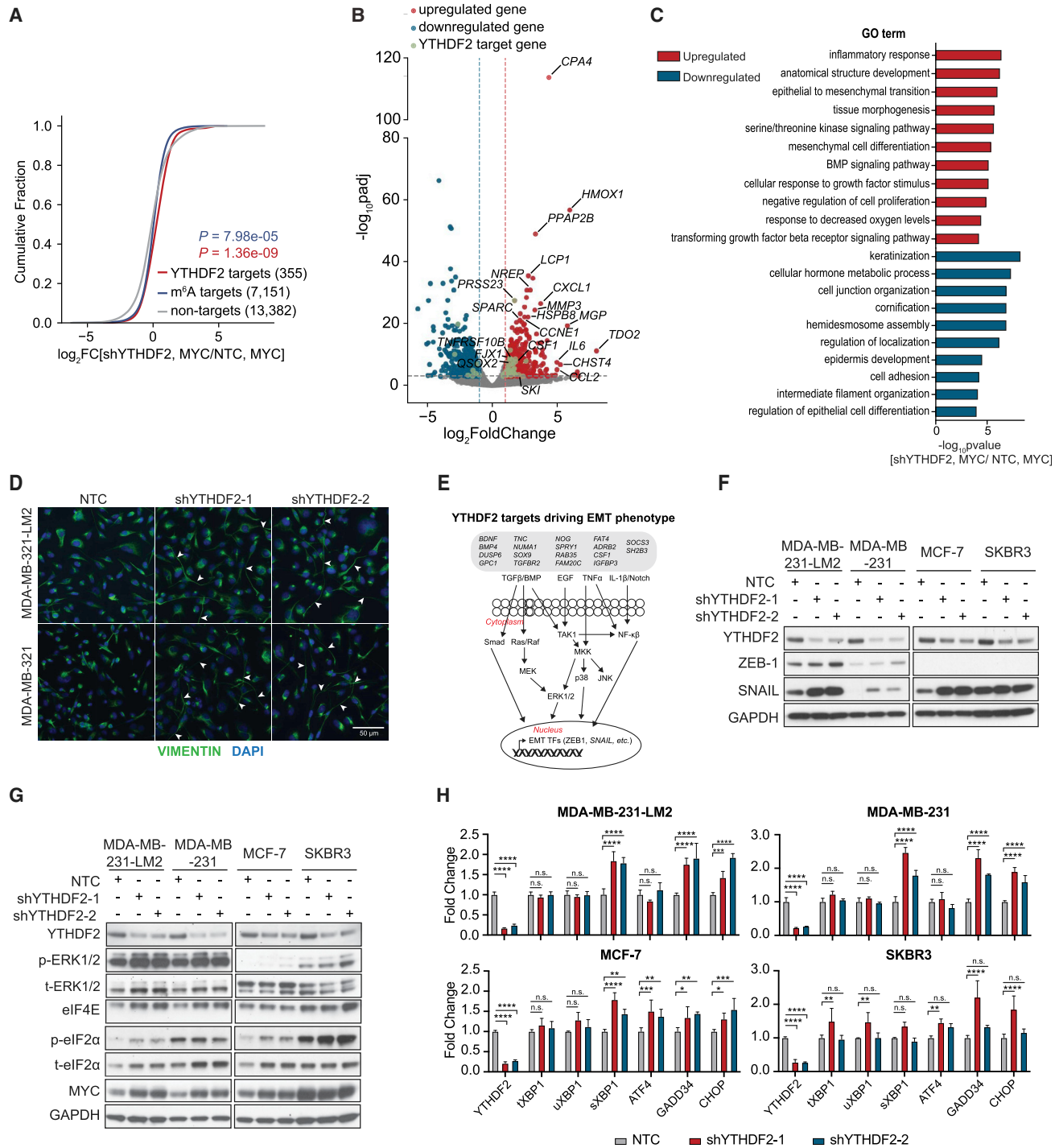


**Figure 4. Depletion of YTHDF2 triggers activation of EMT**

(A) Cumulative distribution of the fold change in mRNA expression of shYTHDF2 cells over non-targeting control (NTC) in MYC-induced HMECs. Two-sided Kolmogorov-Smirnov test compared with non-targets.  $n = 4$  replicates (2 hairpins  $\times$  2 biological replicates).

(B) Volcano plot describing the upregulated (red) and downregulated (blue) genes in shYTHDF2 cells compared with NTC in MYC-induced HMECs. Direct YTHDF2 eCLIP targets are labeled in bold, green text.

(C) Gene Ontology (GO) enrichment of differentially expressed genes in shYTHDF2 cells compared with NTC in MYC-induced HMECs.

(D) Immunofluorescent staining in TNBC cell lines. Arrowheads indicate cell projections. Scale bar, 50  $\mu$ m.

(E) Schematic displaying upstream signaling pathways that induce ERK1/2 signaling and EMT in breast cancer. Overlapping YTHDF2 targets in TNBC cell lines are listed.

(legend continued on next page)

change > 1) were differentially upregulated in YTHDF2-depleted, MYC-induced HMECs compared with NTC (Table S4) and were enriched for ontologies associated with mesenchymal cell transition (i.e., tissue morphogenesis, TGF- $\beta$  receptor signaling, and signaling responses to growth factor stimuli), while downregulated transcripts were enriched for ontologies associated with epithelial cell processes (i.e., adhesion and junction organization, keratinization, and epidermis development) (Figure 4C). In addition, we found that upregulated genes overlapping with those in YTHDF2-depleted MYC-induced HMECs over YTHDF2-depleted uninduced HMECs were enriched for ontologies associated with inflammatory and stress response, but not EMT-specific pathways (Figure S4A), indicating that general inhibition of YTHDF2 promotes EMT and growth factor signaling, but only in conjunction with elevated MYC activity does YTHDF2 inhibition lead to apoptosis.

Supporting this hypothesis, we observed that YTHDF2-depleted TNBC cells displayed a spindle-shape morphology denoted by high levels of vimentin localized to cell projections (Figure 4D). Additionally, we found that several upstream regulators of EMT are YTHDF2 targets (Figure 4E) and that depletion of YTHDF2 resulted in upregulation of the downstream EMT TFs ZEB-1 and SNAIL (Figure 4F). EMT is executed transcriptionally in response to the activation of the MAPK/ERK cascades, often leading to upregulation of MYC itself and increased expression of several translation initiation factors known to contribute to cancer progression (Chen et al., 2013; Truitt et al., 2015; Yin et al., 2017). Following YTHDF2 depletion, we detected ERK1/2 phosphorylation, increased expression of translation initiation factors, and elevated MYC protein expression (Figure 4G). To determine if YTHDF2 limits the activation of signaling pathways operating upstream or in parallel to MYC, we next tested if YTHDF2 regulates MYC's transcriptional targets or the MYC transcript itself. We found that YTHDF2 binding did not always correspond with MYC transcript abundance (Figures S4B and S4C), and although MYC targets were significantly upregulated in YTHDF2-depleted MYC-induced HMECs (Figure S4D), very few significantly upregulated MYC targets were bound by YTHDF2 (Figure S4E). Furthermore, the adaptive endoplasmic reticulum stress pathway is typically engaged during EMT to alleviate metabolic and oxidative stress that accompanies cancer cell transformation and growth by facilitating protein folding and averting cell death (Dey et al., 2013; Feng et al., 2014; Rutkowski et al., 2006). Consistently, we detected activation of the adaptive unfolded protein response (UPR) in all breast cancer subtypes, including upregulation of genes downstream of the serine/threonine PERK kinase, ATF4, GADD34, and CHOP and splicing of XBP1 (sXBP1) downstream of the serine/threonine IRE1 kinase (Figure 4H). In conclusion, we found that depletion of YTHDF2 generally increases the expression of EMT pathway genes in

breast cancer cells, but only TNBC cells were highly sensitive to upregulation of these pathways.

### Depletion of YTHDF2 sensitizes TNBC cells to proteotoxicity

Although it is well established that MYC can actuate both cell proliferation and apoptosis, evidence suggests that rather than inducing apoptosis directly, high levels of MYC expression may be responsible for sensitizing cells to apoptotic triggers (Hart et al., 2012). As depletion of YTHDF2 has recently been shown to sensitize MYC-amplified acute myeloid leukemia (AML) cells to TNF-induced apoptosis (Paris et al., 2019), we next dissected the extrinsic and intrinsic apoptotic pathways driving this phenotype (Figure 5A). Of the most significantly upregulated YTHDF2 target transcripts in YTHDF2-depleted, MYC-induced HMECs, with strong YTHDF2 binding signal centered on m<sup>6</sup>A sites, we first focused on TNF receptor superfamily member 10b (TNFRSF10B; i.e., DR5) (Figure S5A) by probing DR5-induced apoptotic activity through co-depletion of YTHDF2 and DR5. Although we did observe a reduction in caspase-8 cleavage with co-depletion compared with YTHDF2-only-depleted cells, we surprisingly did not observe reduced cleavage of downstream caspase-3, indicating that DR5 knockdown did not halt the apoptotic cascade in YTHDF2-depleted cells (Figure S5B).

As we detected activation of the adaptive UPR in all YTHDF2-depleted breast cancer cells, we hypothesized that the terminal UPR may be activated in YTHDF2-depleted TNBC cells leading to intrinsic apoptosis from excessive endoplasmic reticulum stress (Figure 5A). Indeed, we observed upregulated expression of ER chaperone and foldase proteins, indicating unfolded protein accumulation (Figure S4F), and we detected activation of the c-Jun N-terminal kinase (JNK), resulting in caspase-3 cleavage in TNBC cell lines but not in HR+ or HER2+ cell lines (Figure 5B). Furthermore, unfolded protein accumulation and apoptosis were reversed following treatment with 4-phenylbutyric acid (4-PBA), an endoplasmic reticulum stress inhibitor (Figure S5C), confirming proteotoxicity as the underlying cause of cell death in YTHDF2-depleted TNBC cells. Additionally, cross-reference of public mass spectrometry data for 83 tumor samples provided by the Clinical Proteomic Tumor Analysis Consortium (CPTAC) from TCGA's Cancer Proteome Study of Breast Tissue (Mertins et al., 2016) indicated that YTHDF2 expression is negatively correlated with MAPK activity and that tumor samples with lower YTHDF2 expression have higher levels of ASK1 (MAP3K5), JNK1/2 (MAPK8/9), and p38 (MAPK14) phosphorylation (Figure S5D).

To substantiate that proteotoxicity is a result of disrupting YTHDF2-mediated regulation of its target mRNAs, we identified and modulated the expression of the most significantly upregulated direct YTHDF2 target upon YTHDF2 depletion, serine

(F) Western blot analysis of cell lysates from NTC and shYTHDF2 TNBC, HR+, and HER2+ breast cancer cell lines of EMT transcription factor protein expression. (G) Western blot analysis of cell lysates from NTC and shYTHDF2 TNBC, HR+, and HER2+ breast cancer cell lines of ERK1/2 pathway activation and downstream effectors.

(H) qRT-PCR analysis relative to *GAPDH* of mRNA extracted from shYTHDF2 cells compared with NTC in TNBC, HR+, and HER2+ breast cancer cell lines. \*\*p < 0.01, \*\*\*p < 0.001, and \*\*\*\*p < 0.0001, two-way ANOVA with Dunnett's post hoc test for multiple comparisons. Bars are mean  $\pm$  SD; n = 3 independent replicates. See also Figure S4.

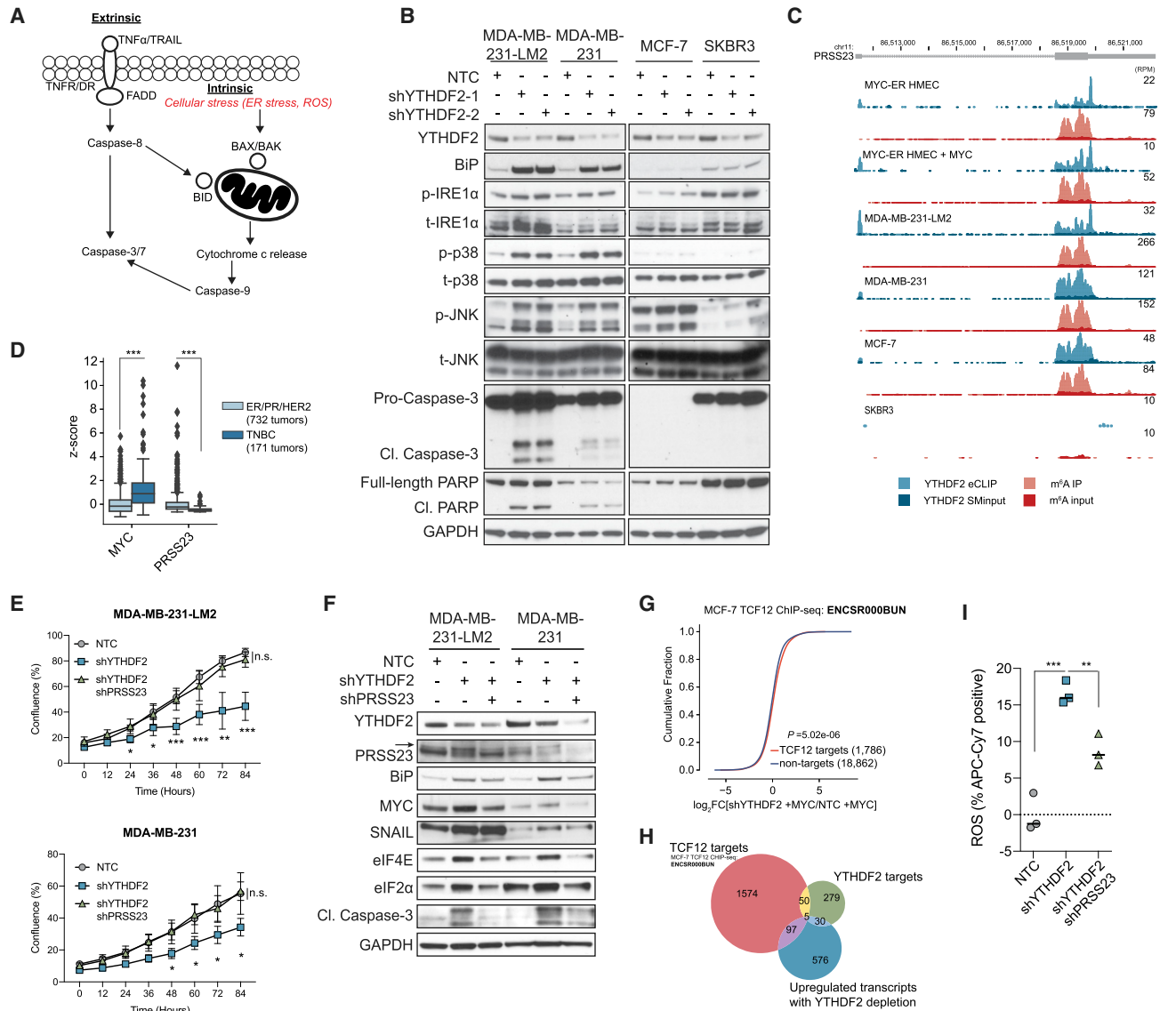


**Figure 5. YTHDF2-depleted TNBC cells initiate apoptosis from intrinsic mitochondrial stress**

(A) Schematic describing the pathways that contribute to extrinsic versus intrinsic apoptosis.

(B) Western blot analysis of cell lysates from non-targeting control (NTC) and shYTHDF2 TNBC, HR+, and HER2+ breast cancer cell lines assessing activation of the terminal unfolded protein response pathway.

(C) Genome Browser tracks (hg19) depicting YTHDF2 eCLIP peaks (light blue) over size-matched (SM) input (dark blue) and m<sup>6</sup>A methylation peaks (light red) over input (dark red) on the *PRSS23* transcript.

(D) Boxplot displaying mRNA expression levels for *MYC* and *PRSS23* in TNBC and ER/PR/HER2-positive tumors from TCGA data portal (Liu et al., 2018). \*\*\*p < 0.001, two-sided Student's t test.

(E) Cell proliferation of shYTHDF2 and YTHDF2/PRSS23 co-depleted TNBC cells. \*p < 0.05, \*\*p < 0.01, \*\*\*p < 0.001, and \*\*\*\*p < 0.0001, two-way ANOVA with Dunnett's post hoc test for multiple comparisons. Values normalized to initial average confluence. Bars are mean  $\pm$  SD; n = 6 independent replicates.

(F) Western blot analysis of cell lysates from shYTHDF2 and YTHDF2/PRSS23 co-depleted TNBC cells assessing protein expression of UPR pathway genes and translation initiation factors.

(G) Cumulative distribution of the fold change in mRNA expression of shYTHDF2 cells over NTC in MYC-induced HMECs. Describes direct TCF12 targets (*ENCSR000BUN*) (red) or non-targets (blue). Two-sided Kolmogorov-Smirnov test compared with non-targets; n = 4 replicates (2 hairpins  $\times$  2 biological replicates).

(H) Venn diagram describing the overlap of TCF12 targets determined in (G) with high-confidence YTHDF2 target genes and differentially upregulated genes in shYTHDF2 MYC-induced HMECs.

(I) Quantification of reactive oxygen species (ROS) in shYTHDF2 and YTHDF2/PRSS23 co-depleted MDA-MB-231-LM2 cells compared with NTC. \*\*p < 0.01 and \*\*\*p < 0.001, one-way ANOVA test with Dunnett's post hoc test for multiple comparisons. Bars represent median values; n = 3 independent replicates.

See also [Figure S5](#).

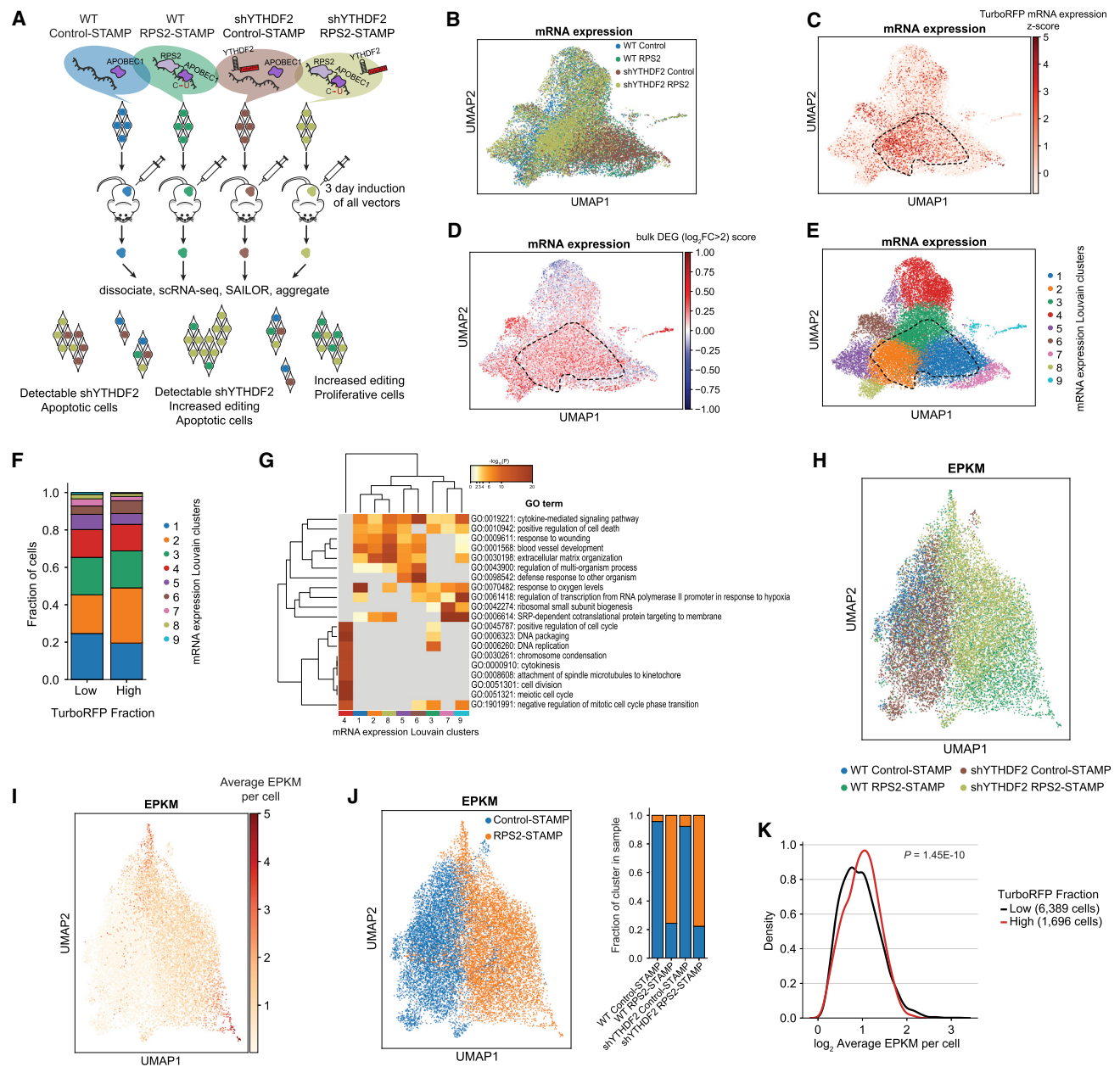


**Figure 6. Analysis of single cells within tumors reveals increased translation rates in YTHDF2-depleted, TurboRFP-tagged cells**

(A) Schematic describing experimental workflow for generating cell lines, engrafting mice and dissociating tumors followed by single cell RNA-seq (scRNA) to profile the transcriptome within tumors.

(B) Uniform manifold approximation and projection (UMAP) analysis of mRNA expression of merged cells from wild-type (WT) control-STAMP cells (blue; n = 6,089), WT RPS2-STAMP cells (green; n = 5,886), shYTHDF2 control-STAMP cells (brown; n = 6,851), and shYTHDF2 RPS2-STAMP cells (yellow; n = 6,630). Experiments performed in MDA-MB-231-LM2 cells.

(C) UMAP analysis of mRNA expression from merged cells from all samples colored by TurboRFP expression. Outline indicates the cluster of highest TurboRFP-expressing cells.

(D) UMAP analysis of mRNA expression from merged cells from all samples colored by expression score of differentially upregulated genes from *in vitro* bulk RNA-seq in shYTHDF2 MYC-induced HMECs (Figure 4B; upregulated). Outline indicates the cluster of highest TurboRFP-expressing cells.

(E) UMAP analysis of mRNA expression from merged cells colored by mRNA expression Louvain clustering. Outline indicates the cluster of highest TurboRFP-expressing cells.

(F) Bar chart describing the fraction of each mRNA expression Louvain cluster in TurboRFP low-expressing (n = 21,464) or high-expressing (n = 3,992) populations. TurboRFP high fraction defined as cells with TurboRFP Z score > 0.

(G) Clustered heatmaps of enriched Gene Ontology (GO) terms extracted from differentially expressed genes belonging to each mRNA expression Louvain cluster (p < 0.05).

(legend continued on next page)

protease 23 (PRSS23) (Figures 4B and 5C). PRSS23 is significantly downregulated in patients with TNBC tumors compared with patients with HR+ or HER2+ tumors (Figure 5D) and co-depletion of YTHDF2 and PRSS23 rescued cell proliferation rates in YTHDF2-depleted TNBC cells (Figure 5E). Additionally, co-depletion of YTHDF2 and PRSS23 produced a substantial reduction in protein levels of translation initiation factors, eIF4E and eIF2 $\alpha$ , MYC and caspase-3 cleavage compared with silencing of YTHDF2 alone (Figure 5F). Previous studies have implicated PRSS23 in translation control (Han et al., 2019a), and PRSS23 localizes to the nucleus and interacts with TCF12, a TF that regulates transcription of genes that promote MYC expression and metastatic phenotypes (Chen et al., 2013; Stelzl et al., 2005; Tang et al., 2019). In agreement with these previous reports, we found that TCF12 targets identified in publicly available chromatin immunoprecipitation sequencing (ChIP-seq) data (ENCODE: ENCSR000BUN) are upregulated in YTHDF2-depleted, MYC-induced HMECs and that the majority of upregulated TCF12 targets are not YTHDF2 targets (Figures 5G and 5H). Moreover, we found that co-depletion of YTHDF2 and PRSS23 partially rescued heat shock protein family A member 5 (BiP) expression (Figure 5F), alleviated reactive oxygen species (ROS) levels by ~50% (Figure 5I), and dampened intrinsic apoptotic signaling (Figure S5B). Moreover, we identified a new facet of regulation by m<sup>6</sup>A in MYC-driven breast cancer where YTHDF2 binds to and targets several transcripts for degradation, including PRSS23, and in doing so safeguards cancer cells from proteotoxicity resulting from excessive endoplasmic reticulum stress.

### Depletion of YTHDF2 boosts translation rates in single cells across tumors

To further test our hypothesis that apoptosis of YTHDF2-depleted TNBC cells is driven by accumulated unfolded proteins, we measured rates of protein synthesis in these cells using puromycin incorporation as a surrogate measure of protein translation. We observed that YTHDF2-depleted cells contained higher levels of puromycin incorporation into nascent peptides, indicating increased levels of protein synthesis (Figure S6A). To substantiate this observation *in vivo*, we leveraged Ribo-STAMP (surveying targets by APOBEC-mediated profiling), a method to assess translation by directing C-to-U base editing of ribosome-bound transcripts using the cytidine deaminase enzyme APOBEC1 fused to the C terminus of the 40S ribosomal protein S2 (RPS2) (Brannan et al., 2021). We generated DOX-inducible, HA-tagged, RPS2-APOBEC1 (RPS2-STAMP), and APOBEC1-only (control-STAMP) expressing cell lines both in wild-type (WT) and in DOX-inducible shRNA-targeting YTHDF2 (TurboRFP-tagged) MDA-MB-231-LM2 cells (Figure S6B). After engraftment, mice were given DOX water for 3 days to induce both shRNA and STAMP transgene

expression prior to tumor resection, dissociation, and single-cell RNA-seq (scRNA-seq) using 10X Chromium Single Cell capture. At this early time point, we uncovered cells harboring molecularly distinct translational signatures driven by both tumor heterogeneity and gene expression changes reflected by C-to-U sequence changes in mRNA (Figure 6A).

Next, we tested if mRNA expression level changes in YTHDF2-depleted single cells resembled our bulk, *in vitro* observations. First, YTHDF2-depleted tumor cell populations (control-STAMP and RPS2-STAMP) contained cells with high raw read coverage in mitochondrial genes compared with WT samples, indicating higher fractions of apoptotic or lysed cells (Figure S6C). Second, uniform manifold approximation and projection (UMAP) visualization of mRNA expression revealed clusters of YTHDF2-depleted tumor cells that were distinct from their WT counterpart (Figure 6B) and cells expressing the TurboRFP tag (TurboRFP<sup>High</sup>) generally had lower YTHDF2 mRNA expression on average compared with cells that did not (TurboRFP<sup>Low</sup>) (Figure S6D). Third, UMAP visualization defined a cell group containing the majority of TurboRFP<sup>High</sup> cells (Figure 6C), which also contained the highest expression of genes that were upregulated in bulk YTHDF2-depleted, MYC-induced HMECs (Figure 6D). This group of cells corresponded to three Louvain mRNA expression clusters (Figure 6E, clusters 1, 2, and 3), with enrichment of TurboRFP<sup>High</sup> cells in cluster 2 (Figure 6F). Fourth, Gene Ontology (GO) analysis of genes from cells assigned to the different mRNA expression Louvain clusters confirmed enrichment for ontologies related to EMT and stress response such as cytokine-mediated signaling, response to wounding, blood vessel development, extracellular matrix (ECM) organization, and positive regulation of cell death in clusters 1 and 2, while clusters 3 and 4 were highly enriched for genes involved in cell cycle progression (Figure 6G). Fifth, in agreement with our *in vitro* studies, we found that clusters 1 and 2 contained larger fractions of cells assigned to G1 phase of the cell cycle on the basis of their transcriptomic expression profiles (Macosko et al., 2015), while cluster 3 was overrepresented for S phase and cluster 4 for G2M phase (Figure S6E). From these analyses, we concluded that the majority of TurboRFP<sup>High</sup> cells undergoing G1 arrest exist in clusters 1 (control-STAMP) and 2 (RPS2-STAMP) and that cluster 3 may contain fewer TurboRFP<sup>High</sup> cells that either have yet to undergo cell-cycle arrest or have not undergone sufficient YTHDF2 depletion to initiate apoptosis, as the mRNA expression profile in cluster 3 more closely resembles that of cluster 4 (Figure 6G), which contains cells expressing proliferative and tumorigenic markers.

Next, we analyzed the translomes of single tumor cells (Brannan et al., 2021) by detecting C-to-U edits on transcripts and assigning site coverage (edited reads per kilobase of

(H) UMAP analysis of unfiltered EPKM of merged cells colored by sample.

(I) UMAP analysis of unfiltered EPKM of merged cells colored by average EPKM per cell.

(J) UMAP analysis of unfiltered EPKM of merged cells colored by EPKM Louvain clustering. Cells filtered on the basis of assignment to control- or RPS2-STAMP cluster. Bar chart describes the fraction of each cluster contained in each sample.

(K) Distribution of control-STAMP filtered, average EPKM per cell for TurboRFP low- and high-expressing populations. TurboRFP<sup>High</sup> fraction defined as cells with TurboRFP Z score > 0. One-sided Kolmogorov-Smirnov test.

See also Figure S6.

transcript per million mapped reads [EPKM]). EPKM from CDS correlated strongly with values from both CDS and 3' UTRs, consistent with the previous observation that 3' UTR signal is specific to RPS2-STAMP-mediated editing (Brannan et al., 2021; Figure S6F). UMAP visualization of EPKM across all tumor samples revealed distinct clustering of control-STAMP samples away from RPS2-STAMP samples (Figures 6H and 6I), and using Louvain clustering by EPKM, we filtered the dataset by excluding cells assigned to the control-STAMP cluster (blue) that did not contain substantial editing (Figure 6J). As transcriptomes and proteomes of individual tumor cells are known to be heterogeneous (Ramon y Cajal et al., 2018), we expected Ribo-STAMP to capture the full spectrum of translational states in tumors regardless of YTHDF2 modulation. Indeed, the distribution of EPKM values for filtered cells revealed a full range of edits throughout the TurboRFP<sup>Low</sup> population (Figure 6K). Generally, we found more edits per gene in the YTHDF2-depleted, TurboRFP<sup>High</sup> population, suggesting increased rates of protein synthesis (Figure 6K).

### scRibo-STAMP identifies unique translation profiles for single YTHDF2-depleted cells within heterogeneous tumors

Tumors are composed of subpopulations of cells that differ at both the genomic and proteomic levels (Ramon y Cajal et al., 2018). Interestingly, we found that in addition to increased rates of protein synthesis, TurboRFP<sup>High</sup> cells also contained edits on more genes per cell on average (Figure S7A), suggesting that YTHDF2 depletion may initiate distinct translation programs. To identify differentially translated mRNAs, we focused on a subpopulation of cells containing the highest number of TurboRFP<sup>High</sup> cells (Figure S7B) with high EPKM (Figure S7C). This group comprised enrichment for cells assigned to cluster 2 (Figure 7A), confirming that many of these cells originated from the shYTHDF2 RPS2-STAMP tumor. Re-visualizing the UMAP space by Louvain clustering on EPKM produced very similar clusters with substantial overlap of mRNA expression-defined cluster 2 with EPKM-defined cluster A (Figures 7A and 7B). This supports our observation that modulation of m<sup>6</sup>A-modified transcripts on the RNA level incites widespread mRNA translation changes. Next, we performed GO analysis of genes from cells assigned to the different EPKM Louvain clusters. Clusters A and C contained the highest number of differentially edited transcripts ( $\geq 99$  genes) and enrichment for TurboRFP<sup>High</sup> cells (Figure 7B), and each cluster respectively corresponded to mRNA expression-defined cluster 2 and clusters 3 and 4 (Figure 7A). Both clusters had high levels of editing within transcripts encoding genes known to contribute globally to translation (Figure 7C). Uniquely, cluster A (“pro-apoptotic” cluster) was enriched for edits within genes involved in apoptosis and antigen presentation, while cluster C (“pro-tumorigenic” cluster) was enriched for edits within genes involved in preventing cell-cycle arrest, homotypic cell adhesion, and dampening oxidative stress, all of which are all associated with tumor progression (Figure 7C). Twenty-six percent of the top 100 differentially edited genes ( $p < 0.05$ ) between EPKM clusters A and C overlapped, while  $\sim 74\%$  were unique to each cluster (Figure 7D). The most highly edited genes in each cluster included cystatin C (CST3) in cluster A

(“pro-apoptotic” cluster), cofilin 1 (CFL1) in cluster C (“pro-tumorigenic” cluster), and 60S ribosomal protein L24 (RPL24) among overlapping genes (Figures 7D and 7E; Table S5). CST3 is a cysteine protease inhibitor that is secreted in response to hypoxia (Rosenow et al., 2013). While being an attractive biomarker in several types of cancers, CST3 is also involved in caspase-mediated cell death (Malone et al., 2020). Conversely, RPL24 is required for polysome assembly and is known to be up-regulated in MYC-driven cancers (Wilson-Edell et al., 2014), and CFL1 is known to drive invasiveness in basal breast cancers (Quintela-Fandino et al., 2010). Accordingly, we found that TNBC tumors generally express significantly higher levels of CFL1 and RPL24 protein and less CST3 protein compared with HR+ and HER2+ tumors (Mertins et al., 2016), supporting a role for CST3 in promoting MYC-driven apoptosis (Figure 7F). In conclusion, Ribo-STAMP data corroborated our findings that YTHDF2-depleted tumor cells contain unique translomes displaying increased translation of tumorigenic and apoptotic transcripts while lacking translation of cell cycle regulators important for maintaining oncogenic proliferation.

### DISCUSSION

Our RBP-focused CRISPR-Cas9 knockout library enabled the systematic discovery of factors involved in multiple stages of RNA processing, including RBPs that regulate transcription, mRNA stability, ribosome recruitment, and translation, as vulnerabilities in MYC-driven breast cancer, generalizing previous reports focusing on splicing (Hsu et al., 2015). Our observations support that deposition of m<sup>6</sup>A on RNA promotes cancer cell growth, survival, and invasion (Lin et al., 2016), and we found that expression of m<sup>6</sup>A reader protein YTHDF2 is required to sustain MYC-driven cell growth and survival in both cells and tumors. Using eCLIP and m<sup>6</sup>A-seq, we identified specific, direct target mRNAs in TNBC cell lines belonging to MAPK/ERK signaling pathways, including several mRNAs encoding upstream activating growth factor and receptor families. Stabilization of these target mRNAs led to upregulation of cellular protein markers of EMT and considerably elevated translation rates, causing endoplasmic reticulum stress from unfolded protein accumulation, culminating in the activation of programmed cell death. As YTHDF2 maintains mRNA homeostasis by limiting the number of translating mRNAs in cancer cells, excessive translation can cause significant cellular stress, particularly in MYC-addicted cells.

YTHDF2 regulates mRNA localization (Ries et al., 2019) and translation (Zhou et al., 2015) in response to various cellular stressors, and previous reports have attributed the function of YTHDF2 in various cancers to the regulation of singular target mRNAs (Chen et al., 2018; Dixit et al., 2021; Paris et al., 2019; Zhong et al., 2019). Our analysis revealed several candidate YTHDF2 targets, and we specifically found that co-depletion of YTHDF2 and its target mRNA, PRSS23, dampened cellular stress that led to the activation of programmed cell death. Nevertheless, our observations suggest that although single target mRNAs may be partially responsible for YTHDF2's effect, a larger subset of its targets may be required for apoptosis in YTHDF2-depleted, MYC-driven breast cancer cells.

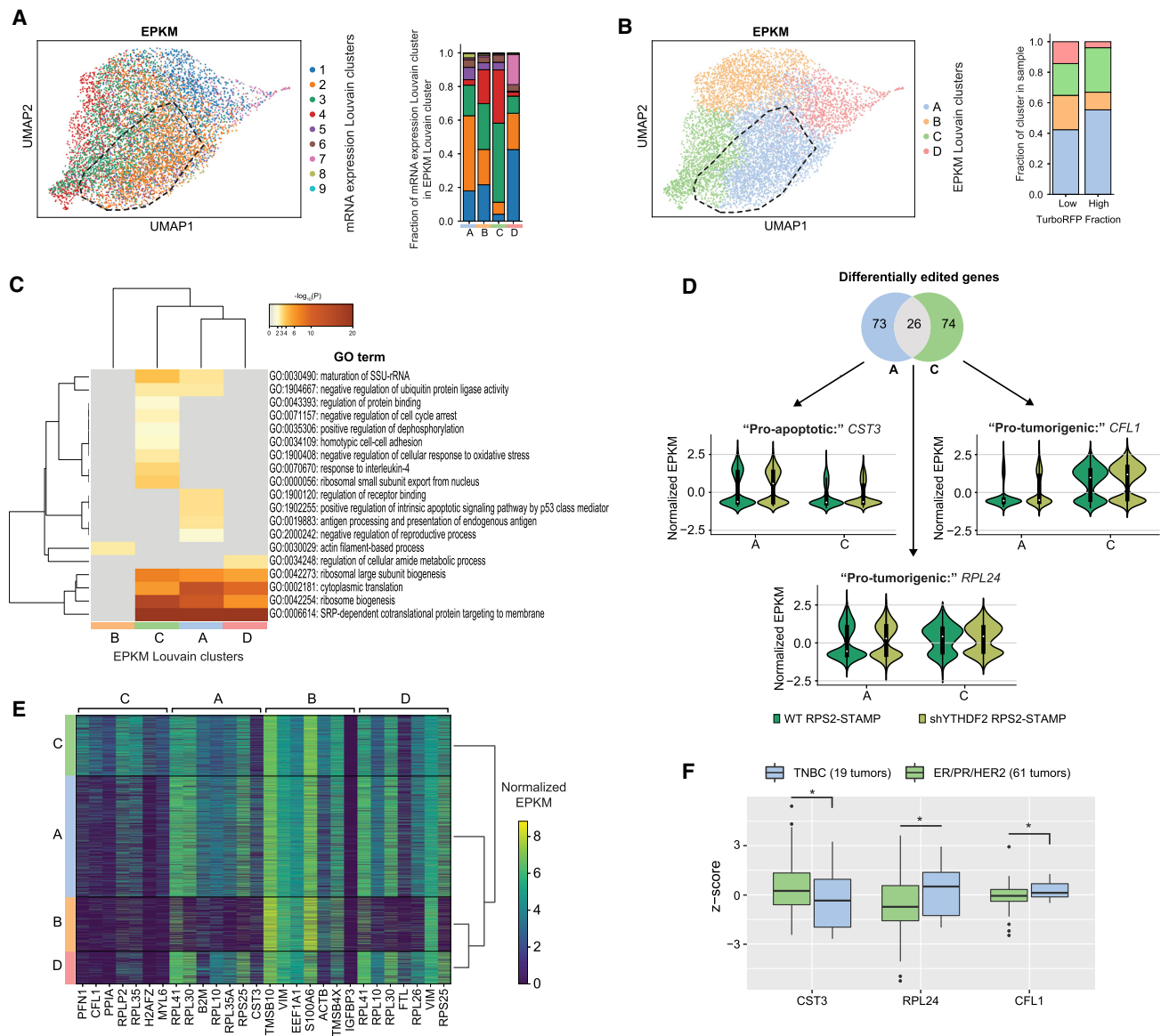


**Figure 7. scRibo-STAMP identifies unique changes in the translome of single cells clustering with TurboRFP-expressing populations**

(A) Uniform manifold approximation and projection (UMAP) analysis of control-STAMP filtered EPKM of merged cells from RPS2-STAMP conditions colored by mRNA expression Louvain clustering. Outline indicates the cluster of highest TurboRFP-expressing cells. Bar chart describes the fraction of each mRNA expression Louvain cluster in each EPKM Louvain cluster.

(B) UMAP analysis of control-STAMP filtered EPKM of merged cells from RPS2-STAMP samples colored by EPKM Louvain clustering. Outline indicates the cluster of highest TurboRFP-expressing cells. Bar chart describes the fraction of each EPKM Louvain cluster contained in TurboRFP high-expressing ( $n = 1,696$ ) and low-expressing ( $n = 6,389$ ) populations.

(C) Clustered heatmaps of enriched Gene Ontology (GO) terms extracted from differentially edited genes from each EPKM Louvain cluster ( $p < 0.05$ ).

(D) Venn diagram overlaps of differentially edited genes between EPKM Louvain clusters A (*CST3*), EPKM Louvain cluster C (*CFL1*) or both (*RPL24*). Cluster A,  $n = 3,656$ ; cluster C,  $n = 1,823$ .

(E) Heatmap of normalized EPKM signatures for merged RPS2-STAMP cells for the top seven differentially edited genes per EPKM Louvain cluster.

(F) Boxplot comparing protein expression levels for *CST3*, *RPL24*, and *CFL1* between TNBC and ER/PR/HER2-positive tumors downloaded from TCGA's Cancer Proteome Study of Breast Tissue (Mertins et al., 2016). \* $p < 0.05$ , one-sided Student's t test.

See also Figure S7.

Here, we applied scRibo-STAMP to measure mRNA translation in individual tumor cells, which to our knowledge remains an outstanding challenge. scRibo-STAMP enabled the simultaneous quantification of transcriptomic and translational changes and pro-

vided an early snapshot of changes occurring within tumor cells following YTHDF2 depletion and prior to widespread apoptosis. Our dataset captured tumor cells in distinct states characterized by cell cycle phase, proliferation, and tumorigenesis. We observed

increased editing on transcripts encoding secreted proteins regulating ECM composition in YTHDF2-depleted cells, which are known to be produced during EMT and metastasis and suggests mechanisms underlying crosstalk among cells with different levels of YTHDF2 expression. Our single-cell studies demonstrate the utility of scRibo-STAMP to reveal snapshots of translational landscapes and underlying gene expression profiles at critical periods in cancer progression.

Our results indicate that YTHDF2 is essential for the survival of TNBC cells to limit the availability of methylated transcripts during constitutively elevated levels of transcription and translation in cells with aberrantly high MYC activity, while it is dispensable for cells that are less reliant on elevated MYC expression. Our model is supported by gene expression analyses of TNBC tumors linking low YTHDF2 expression levels to longer patient survival rates, and we demonstrate the efficacy and feasibility of depleting YTHDF2 as a potential therapeutic strategy by generating viable adult-life inducible systemic *Ythdf2*-knockout mice. Finally, recent evidence indicates that YTH paralogs may play compensatory roles for one another, providing anticipation for minimal adverse side effects to YTHDF2 inhibition (Lasman et al., 2020; Zaccara and Jaffrey, 2020). Altogether, our studies reveal disease-promoting RBP-RNA interactions that are selectively essential for growth and survival of tumor cells but not somatic tissues and that targeting RBPs holds great promise for minimally toxic and highly specific treatment modalities in specific cancer subtypes.

### Limitations of study

Although we used an isogenic cell line to interrogate RBP vulnerabilities in MYC-driven cancer, the cell line was derived from HMECs, and all subsequent studies were performed using breast cancer cell lines of different subtypes. We did not elect to generalize our observations to cancers originating from tissues other than breast, but several studies support our finding that YTHDF2 depletion triggers apoptosis in MYC-driven cancer cells. For example, an apoptotic phenotype was observed following YTHDF2 depletion in the AML cell line THP-1 (Paris et al., 2019), prostate cancer cell lines DU-145 and PC3 (Li et al., 2017), and ovarian cancer cell line SKOV3 (Li et al., 2020), all of which are highly sensitive to MYC depletion (Ai et al., 2013; Fan et al., 2016; Huang et al., 2014). Nevertheless, additional experimentation in MYC-amplified and MYC-normal cancer cell lines derived from different tissues of origin are necessary to generalize our findings across all MYC-driven cancers.

### STAR★METHODS

Detailed methods are provided in the online version of this paper and include the following:

- **KEY RESOURCES TABLE**
- **RESOURCE AVAILABILITY**
  - Lead contact
  - Materials availability
  - Data and code availability
- **EXPERIMENTAL MODEL AND SUBJECT DETAILS**
  - Cell lines and cell culture
  - Animal studies

### ● METHOD DETAILS

- Lentivirus production and purification
- Multiplicity of infection
- MYC-ER HMEC RBP CRISPR screen
- Bulk sgRNA library preparation
- Knockdown experiments
- Annexin V/ PI apoptosis assay
- Cell cycle analysis
- Pooled *in vivo* shRNA screen and analysis
- *In vivo* tumorigenicity assays
- Immunohistochemistry
- Immunofluorescence
- eCLIP-seq library preparation and analysis
- m<sup>6</sup>A-seq library preparation and analysis
- RNA-seq library preparation and analysis
- Western blot
- SUnSET assay
- ER stress inhibition assay
- Cellular ROS assay
- qRT-PCR analysis
- Gene Ontology (GO) analysis
- Time lapse microscopy
- TCGA data description
- scRibo-STAMP assays and analysis

### ● QUANTIFICATION AND STATISTICAL ANALYSIS

### SUPPLEMENTAL INFORMATION

Supplemental information can be found online at <https://doi.org/10.1016/j.molcel.2021.06.014>.

### ACKNOWLEDGMENTS

We thank Prof. Chuan He (University of Chicago) for the generous gift of *Ythdf2*<sup>fl/fl</sup> mice. We are grateful to Dr. Kristopher Brannan and Ryan Marina in the Yeo lab for providing reagents and guidance on implementing STAMP. We thank the Sanford Consortium Human Embryonic Stem Cell Core and the University of California (UC) San Diego Stem Cell Genomics Core for providing us use of their instruments and cell-sorting services (1S100D025060). We acknowledge the Tissue Technology Shared Resource at the Moores Cancer Center for histology processing. This publication includes data generated using an Illumina NovaSeq 6000 at UC San Diego provided by the IGM Genomics Center (S100D026929). Data used in this publication were generated by the CPTAC (National Cancer Institute [NCI]/NIH) (Liu et al., 2018; Mertins et al., 2016). The results published here are based in part upon data generated by TCGA Research Network (<https://www.cancer.gov/about-nci/organization/ccg/research/structural-genomics/tcga>). CHIP-seq datasets were downloaded from the ENCODE portal (Sloan et al., 2016) with the identifiers ENCODE: ENCSR000DOS and ENCODE: ENCSR000BUN. J.M.E. is supported by the Ruth L. Kirschstein F31 National Research Service Award (F31 CA217173) from the NIH and the Cancer Systems Biology Training Program (P50 GM085764 and U54 CA209891). M.P. is supported by the Ruth L. Kirschstein F32 National Research Service Award (F32 HL143978) from the NIH. I.A.C. is a UC San Diego Chancellor's Postdoctoral Fellow and a San Diego Institutional Research and Academic Career Development Award (IRACDA) Fellow supported by NIH/National Institute of General Medical Sciences (NIGMS) (K12 GM068524). J.K.M. is supported by the Susan G. Komen PDF Basic/Translational and Clinical Funding Program (PDF17487931). T.F.W. is supported by the NIH and NCI (U01CA214125, 1R01CA215226, and 1R01CA215452), the US Department of Defense (DOD) (1W81XWH-18-1-0573), the McNair Medical Institute, the Cancer Research UK (CRUK) Grand Challenge, and the Mark Foundation For Cancer Research (C5470/A27144 to T.F.W. as a

member of the SPECIFICANCER Team). This study was partially supported by NIH grants HG009889, HG004659, AI123202, and AI132122 to G.W.Y.

#### AUTHOR CONTRIBUTIONS

Conceptualization, J.M.E., T.F.W., and G.W.Y.; methodology, J.M.E., M.P., and J.K.M.; software, B.A.Y.; formal analysis, J.M.E., I.A.C., J.K.N., H.L., and N.J.N.; investigation, J.M.E., M.P., J.K.M., A.T.T., and A.A.M.; resources, A.S., and S.T.; data curation, J.M.E., I.A.C., J.K.N., and N.J.N.; writing – original draft, J.M.E.; writing – review & editing, J.M.E., M.P., and G.W.Y.; visualization, J.M.E., I.A.C., and J.K.M.; supervision, T.F.W. and G.W.Y.; funding acquisition, T.F.W. and G.W.Y.

#### DECLARATION OF INTERESTS

G.W.Y. is a co-founder, a member of the board of directors, an equity holder, on the scientific advisory board (SAB), and a paid consultant for Locanabio and Eclipse BioInnovations. G.W.Y. is also a visiting faculty member at the National University of Singapore. The terms of this arrangement have been reviewed and approved by UC San Diego in accordance with its conflict-of-interest policies. J.M.E. and G.W.Y. are inventors on a patent disclosure at UC San Diego related to this work. The authors declare no other competing interests.

Received: November 3, 2020

Revised: March 11, 2021

Accepted: June 10, 2021

Published: July 2, 2021

#### REFERENCES

Ai, Z.H., Wang, J., Xu, Y.L., Zhu, X.L., and Teng, Y.C. (2013). Suppression of RNA interference on expression of c-myc of SKOV3 ovarian carcinoma cell line. *Eur. Rev. Med. Pharmacol. Sci.* **17**, 3002–3006.

Brannan, K.W., Chaim, I.A., Marina, R.J., Yee, B.A., Kofman, E.R., Lorenz, D.A., Jagannatha, P., Dong, K.D., Madrigal, A.A., Underwood, J.G., and Yeo, G.W. (2021). Robust single-cell discovery of RNA targets of RNA-binding proteins and ribosomes. *Nat. Methods* **18**, 507–519.

Chen, I.H., Wang, H.H., Hsieh, Y.S., Huang, W.C., Yeh, H.I., and Chuang, Y.J. (2013). PRSS23 is essential for the Snail-dependent endothelial-to-mesenchymal transition during valvulogenesis in zebrafish. *Cardiovasc. Res.* **97**, 443–453.

Chen, M., Wei, L., Law, C.T., Tsang, F.H., Shen, J., Cheng, C.L., Tsang, L.H., Ho, D.W., Chiu, D.K., Lee, J.M., et al. (2018). RNA N6-methyladenosine methyltransferase-like 3 promotes liver cancer progression through YTHDF2-dependent posttranscriptional silencing of SOCS2. *Hepatology* **67**, 2254–2270.

Danecek, P., Bonfield, J.K., Liddle, J., Marshall, J., Ohan, V., Pollard, M.O., Whitwham, A., Keane, T., McCarthy, S.A., Davies, R.M., and Li, H. (2021). Twelve years of SAMtools and BCFtools. *Gigascience* **10**, giab008.

Deffit, S.N., Yee, B.A., Manning, A.C., Rajendren, S., Vadlamani, P., Wheeler, E.C., Domissy, A., Washburn, M.C., Yeo, G.W., and Hundley, H.A. (2017). The *C. elegans* neural editome reveals an ADAR target mRNA required for proper chemotaxis. *eLife* **6**, e28625.

Dey, S., Tameire, F., and Koumenis, C. (2013). PERK-ing up autophagy during MYC-induced tumorigenesis. *Autophagy* **9**, 612–614.

Dixit, D., Prager, B.C., Gimple, R.C., Poh, H.X., Wang, Y., Wu, Q., Qiu, Z., Kidwell, R.L., Kim, L.J.Y., Xie, Q., et al. (2021). The RNA m6A reader YTHDF2 maintains oncogene expression and is a targetable dependency in glioblastoma stem cells. *Cancer Discov.* **11**, 480–499.

Dobin, A., Davis, C.A., Schlesinger, F., Drenkow, J., Zaleski, C., Jha, S., Batut, P., Chaisson, M., and Gingeras, T.R. (2013). STAR: ultrafast universal RNA-seq aligner. *Bioinformatics* **29**, 15–21.

Dominissini, D., Moshitch-Moshkovitz, S., Salmon-Divon, M., Amariglio, N., and Rechavi, G. (2013). Transcriptome-wide mapping of N(6)-methyladeno-

sine by m(6)A-seq based on immunocapturing and massively parallel sequencing. *Nat. Protoc.* **8**, 176–189.

Du, H., Zhao, Y., He, J., Zhang, Y., Xi, H., Liu, M., Ma, J., and Wu, L. (2016). YTHDF2 destabilizes m(6)A-containing RNA through direct recruitment of the CCR4-NOT deadenylase complex. *Nat. Commun.* **7**, 12626.

Eden, E., Navon, R., Steinfeld, I., Lipson, D., and Yakhini, Z. (2009). GOrilla: a tool for discovery and visualization of enriched GO terms in ranked gene lists. *BMC Bioinformatics* **10**, 48.

Fan, L., Peng, G., Sahgal, N., Fazli, L., Gleave, M., Zhang, Y., Hussain, A., and Qi, J. (2016). Regulation of c-Myc expression by the histone demethylase JMJD1A is essential for prostate cancer cell growth and survival. *Oncogene* **35**, 2441–2452.

Feng, Y.X., Sokol, E.S., Del Vecchio, C.A., Sanduja, S., Claessen, J.H., Proia, T.A., Jin, D.X., Reinhardt, F., Ploegh, H.L., Wang, Q., and Gupta, P.B. (2014). Epithelial-to-mesenchymal transition activates PERK-eIF2 $\alpha$  and sensitizes cells to endoplasmic reticulum stress. *Cancer Discov.* **4**, 702–715.

Green, A.R., Aleskandarany, M.A., Agarwal, D., Elsheikh, S., Nolan, C.C., Diez-Rodriguez, M., Macmillan, R.D., Ball, G.R., Caldas, C., Madhusudan, S., et al. (2016). MYC functions are specific in biological subtypes of breast cancer and confers resistance to endocrine therapy in luminal tumours. *Br. J. Cancer* **114**, 917–928.

Han, B., Yang, Y., Chen, J., He, X., Lv, N., and Yan, R. (2019a). PRSS23 knock-down inhibits gastric tumorigenesis through EIF2 signaling. *Pharmacol. Res.* **142**, 50–57.

Han, H., Jain, A.D., Truica, M.I., Izquierdo-Ferrer, J., Anker, J.F., Lysy, B., Sagar, V., Luan, Y., Chalmers, Z.R., Unno, K., et al. (2019b). Small-molecule MYC inhibitors suppress tumor growth and enhance immunotherapy. *Cancer Cell* **36**, 483–497.e15.

Handa, T., Katayama, A., Yokobori, T., Yamane, A., Fujii, T., Obayashi, S., Kurozumi, S., Kawabata-Iwakawa, R., Gombodorj, N., Nishiyama, M., et al. (2019). Carboxypeptidase A4 accumulation is associated with an aggressive phenotype and poor prognosis in triple-negative breast cancer. *Int. J. Oncol.* **54**, 833–844.

Hart, L.S., Cunningham, J.T., Datta, T., Dey, S., Tameire, F., Lehman, S.L., Qiu, B., Zhang, H., Cerniglia, G., Bi, M., et al. (2012). ER stress-mediated autophagy promotes Myc-dependent transformation and tumor growth. *J. Clin. Invest.* **122**, 4621–4634.

He, X., Arslan, A.D., Ho, T.T., Yuan, C., Stampfer, M.R., and Beck, W.T. (2014). Involvement of polypyrimidine tract-binding protein (PTBP1) in maintaining breast cancer cell growth and malignant properties. *Oncogenesis* **3**, e84.

Heinz, S., Benner, C., Spann, N., Bertolino, E., Lin, Y.C., Laslo, P., Cheng, J.X., Murre, C., Singh, H., and Glass, C.K. (2010). Simple combinations of lineage-determining transcription factors prime cis-regulatory elements required for macrophage and B cell identities. *Mol. Cell* **38**, 576–589.

Hentze, M.W., Castello, A., Schwarzl, T., and Preiss, T. (2018). A brave new world of RNA-binding proteins. *Nat. Rev. Mol. Cell Biol.* **19**, 327–341.

Hsu, T.Y., Simon, L.M., Neill, N.J., Marcotte, R., Sayad, A., Bland, C.S., Echeverria, G.V., Sun, T., Kurley, S.J., Tyagi, S., et al. (2015). The spliceosome is a therapeutic vulnerability in MYC-driven cancer. *Nature* **525**, 384–388.

Huang, X., Spencer, G.J., Lynch, J.T., Ciceri, F., Somerville, T.D., and Somerville, T.C. (2014). Enhancers of Polycomb EPC1 and EPC2 sustain the oncogenic potential of MLL leukemia stem cells. *Leukemia* **28**, 1081–1091.

Huang, H., Weng, H., Sun, W., Qin, X., Shi, H., Wu, H., Zhao, B.S., Mesquita, A., Liu, C., Yuan, C.L., et al. (2018). Recognition of RNA N<sup>6</sup>-methyladenosine by IGF2BP proteins enhances mRNA stability and translation. *Nat. Cell Biol.* **20**, 285–295.

Ivanova, I., Much, C., Di Giacomo, M., Azzi, C., Morgan, M., Moreira, P.N., Monahan, J., Carrieri, C., Enright, A.J., and O'Carroll, D. (2017). The RNA m<sup>6</sup>A reader YTHDF2 is essential for the post-transcriptional regulation of the maternal transcriptome and oocyte competence. *Mol. Cell* **67**, 1059–1067.e4.

Kessler, J.D., Kahle, K.T., Sun, T., Meerbrey, K.L., Schlabach, M.R., Schmitt, E.M., Skinner, S.O., Xu, Q., Li, M.Z., Hartman, Z.C., et al. (2012).

- A SUMOylation-dependent transcriptional subprogram is required for Myc-driven tumorigenesis. *Science* 335, 348–353.
- Lafon, I., Carballès, F., Brewer, G., Poiret, M., and Morello, D. (1998). Developmental expression of AUF1 and HuR, two c-myc mRNA binding proteins. *Oncogene* 16, 3413–3421.
- Lambert, N., Robertson, A., Jangi, M., McGeary, S., Sharp, P.A., and Burge, C.B. (2014). RNA Bind-n-Seq: quantitative assessment of the sequence and structural binding specificity of RNA binding proteins. *Mol. Cell* 54, 887–900.
- Lan, Q., Liu, P.Y., Haase, J., Bell, J.L., Hüttelmaier, S., and Liu, T. (2019). The critical role of RNA m<sup>6</sup>A methylation in cancer. *Cancer Res.* 79, 1285–1292.
- Langmead, B., and Salzberg, S.L. (2012). Fast gapped-read alignment with Bowtie 2. *Nat. Methods* 9, 357–359.
- Lasman, L., Krupalnik, V., Viukov, S., Mor, N., Aguilera-Castrejon, A., Schneir, D., Bayerl, J., Mizrahi, O., Peles, S., Tawil, S., et al. (2020). Context-dependent functional compensation between Ythdf m<sup>6</sup>A reader proteins. *Genes Dev.* 34, 1373–1391.
- Li, W., Xu, H., Xiao, T., Cong, L., Love, M.I., Zhang, F., Irizarry, R.A., Liu, J.S., Brown, M., and Liu, X.S. (2014). MAGeCK enables robust identification of essential genes from genome-scale CRISPR/Cas9 knockout screens. *Genome Biol.* 15, 554.
- Li, J., Meng, S., Xu, M., Wang, S., He, L., Xu, X., Wang, X., and Xie, L. (2017). Downregulation of N<sup>6</sup>-methyladenosine binding YTHDF2 protein mediated by miR-493-3p suppresses prostate cancer by elevating N<sup>6</sup>-methyladenosine levels. *Oncotarget* 9, 3752–3764.
- Li, Z., Qian, P., Shao, W., Shi, H., He, X.C., Gogol, M., Yu, Z., Wang, Y., Qi, M., Zhu, Y., et al. (2018). Suppression of m<sup>6</sup>A reader Ythdf2 promotes hematopoietic stem cell expansion. *Cell Res.* 28, 904–917.
- Li, J., Wu, L., Pei, M., and Zhang, Y. (2020). YTHDF2, a protein repressed by miR-145, regulates proliferation, apoptosis, and migration in ovarian cancer cells. *J. Ovarian Res.* 13, 111.
- Liao, Y., Smyth, G.K., and Shi, W. (2014). featureCounts: an efficient general purpose program for assigning sequence reads to genomic features. *Bioinformatics* 30, 923–930.
- Lin, S., Choe, J., Du, P., Triboulet, R., and Gregory, R.I. (2016). The m<sup>6</sup>A methyltransferase METTL3 promotes translation in human cancer cells. *Mol. Cell* 62, 335–345.
- Liu, J., Lichtenberg, T., Hoadley, K.A., Poisson, L.M., Lazar, A.J., Cherniack, A.D., Kovatich, A.J., Benz, C.C., Levine, D.A., Lee, A.V., et al.; Cancer Genome Atlas Research Network (2018). An integrated TCGA pan-cancer clinical data resource to drive high-quality survival outcome analytics. *Cell* 173, 400–416.e11.
- Love, M.I., Huber, W., and Anders, S. (2014). Moderated estimation of fold change and dispersion for RNA-seq data with DESeq2. *Genome Biol.* 15, 550.
- Macosko, E.Z., Basu, A., Satija, R., Nemes, J., Shekhar, K., Goldman, M., Tirosh, I., Bialas, A.R., Kamitaki, N., Martersteck, E.M., et al. (2015). Highly parallel genome-wide expression profiling of individual cells using nanoliter droplets. *Cell* 161, 1202–1214.
- Malone, M.K., Smrekar, K., Park, S., Blakely, B., Walter, A., Nasta, N., Park, J., Considine, M., Danilova, L.V., Pandey, N.B., et al. (2020). Cytokines secreted by stromal cells in TNBC microenvironment as potential targets for cancer therapy. *Cancer Biol. Ther.* 21, 560–569.
- Martin, M. (2011). Cutadapt removes adapter sequences from high-throughput sequencing reads. *EMBnet. J.* 17 (1).
- Mayr, C., and Bartel, D.P. (2009). Widespread shortening of 3'UTRs by alternative cleavage and polyadenylation activates oncogenes in cancer cells. *Cell* 138, 673–684.
- Meerbrey, K.L., Hu, G., Kessler, J.D., Roarty, K., Li, M.Z., Fang, J.E., Herschkowitz, J.I., Burrows, A.E., Ciccio, A., Sun, T., et al. (2011). The pINDUCER lentiviral toolkit for inducible RNA interference in vitro and in vivo. *Proc. Natl. Acad. Sci. U S A* 108, 3665–3670.
- Mertins, P., Mani, D.R., Ruggles, K.V., Gillette, M.A., Clauser, K.R., Wang, P., Wang, X., Qiao, J.W., Cao, S., Petralia, F., et al.; NCI CPTAC (2016). Proteogenomics connects somatic mutations to signalling in breast cancer. *Nature* 534, 55–62.
- Minn, A.J., Gupta, G.P., Siegel, P.M., Bos, P.D., Shu, W., Giri, D.D., Viale, A., Olshen, A.B., Gerald, W.L., and Massagué, J. (2005). Genes that mediate breast cancer metastasis to lung. *Nature* 436, 518–524.
- Olarerin-George, A.O., and Jaffrey, S.R. (2017). MetaPlotR: a Perl/R pipeline for plotting metagenes of nucleotide modifications and other transcriptomic sites. *Bioinformatics* 33, 1563–1564.
- Paris, J., Morgan, M., Campos, J., Spencer, G.J., Shmakova, A., Ivanova, I., Mapperley, C., Lawson, H., Wotherspoon, D.A., Sepulveda, C., et al. (2019). Targeting the RNA m<sup>6</sup>A reader YTHDF2 selectively compromises cancer stem cells in acute myeloid leukemia. *Cell Stem Cell* 25, 137–148.e6.
- Park, S., Brugiolo, M., Akerman, M., Das, S., Urbanski, L., Geier, A., Kesarwani, A.K., Fan, M., Leclair, N., Lin, K.T., et al. (2019). Differential functions of splicing factors in mammary transformation and breast cancer metastasis. *Cell Rep.* 29, 2672–2688.e7.
- Pereira, B., Billaud, M., and Almeida, R. (2017). RNA-binding proteins in cancer: old players and new actors. *Trends Cancer* 3, 506–528.
- Quintela-Fandino, M., Arpaia, E., Brenner, D., Goh, T., Yeung, F.A., Blaser, H., Alexandrova, R., Lind, E.F., Tusche, M.W., Wakeham, A., et al. (2010). HUNK suppresses metastasis of basal type breast cancers by disrupting the interaction between PP2A and cofilin-1. *Proc. Natl. Acad. Sci. U S A* 107, 2622–2627.
- Ramon y Cajal, S., Castellvi, J., Hümmer, S., Peg, V., Pelletier, J., and Sonenberg, N. (2018). Beyond molecular tumor heterogeneity: protein synthesis takes control. *Oncogene* 37, 2490–2501.
- Ries, R.J., Zaccara, S., Klein, P., Olarerin-George, A., Namkoong, S., Pickering, B.F., Patil, D.P., Kwak, H., Lee, J.H., and Jaffrey, S.R. (2019). m<sup>6</sup>A enhances the phase separation potential of mRNA. *Nature* 571, 424–428.
- Rosenow, A., Noben, J.P., Bouwman, F.G., Mariman, E.C., and Renes, J. (2013). Hypoxia-mimetic effects in the secretome of human preadipocytes and adipocytes. *Biochim. Biophys. Acta* 1834, 2761–2771.
- Rutkowski, D.T., Arnold, S.M., Miller, C.N., Wu, J., Li, J., Gunnison, K.M., Mori, K., Sadighi Akha, A.A., Raden, D., and Kaufman, R.J. (2006). Adaptation to ER stress is mediated by differential stabilities of pro-survival and pro-apoptotic mRNAs and proteins. *PLoS Biol.* 4, e374.
- Shalem, O., Sanjana, N.E., Hartenian, E., Shi, X., Scott, D.A., Mikkelsen, T., Heckl, D., Ebert, B.L., Root, D.E., Doench, J.G., and Zhang, F. (2014). Genome-scale CRISPR-Cas9 knockout screening in human cells. *Science* 343, 84–87.
- Sloan, C.A., Chan, E.T., Davidson, J.M., Malladi, V.S., Strattan, J.S., Hitz, B.C., Gabdank, I., Narayanan, A.K., Ho, M., Lee, B.T., et al. (2016). ENCODE data at the ENCODE portal. *Nucleic Acids Res.* 44 (D1), D726–D732.
- Stelzl, U., Worm, U., Lalowski, M., Haenig, C., Brembeck, F.H., Goehler, H., Stroedicke, M., Zenkner, M., Schoenherr, A., Koeppen, S., et al. (2005). A human protein-protein interaction network: a resource for annotating the proteome. *Cell* 122, 957–968.
- Struntz, N.B., Chen, A., Deutzmann, A., Wilson, R.M., Stefan, E., Evans, H.L., Ramirez, M.A., Liang, T., Caballero, F., Wildschut, M.H.E., et al. (2019). Stabilization of the Max homodimer with a small molecule attenuates Myc-driven transcription. *Cell Chem. Biol.* 26, 711–723.e14.
- Tang, X., Tu, G., Yang, G., Wang, X., Kang, L., Yang, L., Zeng, H., Wan, X., Qiao, Y., Cui, X., et al. (2019). Autocrine TGF- $\beta$ 1/miR-200s/miR-221/DNMT3B regulatory loop maintains CAF status to fuel breast cancer cell proliferation. *Cancer Lett.* 452, 79–89.
- Truitt, M.L., Conn, C.S., Shi, Z., Pang, X., Tokuyasu, T., Coady, A.M., Seo, Y., Barna, M., and Ruggero, D. (2015). Differential requirements for eIF4E dose in normal development and cancer. *Cell* 162, 59–71.
- Van Nostrand, E.L., Nguyen, T.B., Gelboin-Burkhardt, C., Wang, R., Blue, S.M., Pratt, G.A., Louie, A.L., and Yeo, G.W. (2017). Robust, cost-effective profiling of RNA binding protein targets with single-end enhanced crosslinking and immunoprecipitation (seCLIP). *Methods Mol. Biol.* 1648, 177–200.
- Wan, C., Gong, C., Zhang, H., Hua, L., Li, X., Chen, X., Chen, Y., Ding, X., He, S., Cao, W., et al. (2016).  $\beta$ 2-adrenergic receptor signaling promotes

- pancreatic ductal adenocarcinoma (PDAC) progression through facilitating PCBP2-dependent c-myc expression. *Cancer Lett.* **373**, 67–76.
- Wang, X., Lu, Z., Gomez, A., Hon, G.C., Yue, Y., Han, D., Fu, Y., Parisien, M., Dai, Q., Jia, G., et al. (2014). N6-methyladenosine-dependent regulation of messenger RNA stability. *Nature* **505**, 117–120.
- Wheeler, E.C., Vu, A.Q., Einstein, J.M., DiSalvo, M., Ahmed, N., Van Nostrand, E.L., Shishkin, A.A., Jin, W., Allbritton, N.L., and Yeo, G.W. (2020). Pooled CRISPR screens with imaging on microarray reveals stress granule-regulatory factors. *Nat. Methods* **17**, 636–642.
- Wilson-Edell, K.A., Kehasse, A., Scott, G.K., Yau, C., Rothschild, D.E., Schilling, B., Gabriel, B.S., Yevtushenko, M.A., Hanson, I.M., Held, J.M., et al. (2014). RPL24: a potential therapeutic target whose depletion or acetylation inhibits polysome assembly and cancer cell growth. *Oncotarget* **5**, 5165–5176.
- Wolf, F.A., Angerer, P., and Theis, F.J. (2018). SCANPY: large-scale single-cell gene expression data analysis. *Genome Biol.* **19**, 15.
- Yin, S., Cheryan, V.T., Xu, L., Rishi, A.K., and Reddy, K.B. (2017). Myc mediates cancer stem-like cells and EMT changes in triple negative breast cancers cells. *PLoS ONE* **12**, e0183578.
- Zaccara, S., and Jaffrey, S.R. (2020). A unified model for the function of YTHDF proteins in regulating m(6)A-modified mRNA. *Cell* **181**, 1582–1595.
- Zhang, Y., Liu, T., Meyer, C.A., Eeckhoutte, J., Johnson, D.S., Bernstein, B.E., Nusbaum, C., Myers, R.M., Brown, M., Li, W., and Liu, X.S. (2008). Model-based analysis of ChIP-seq (MACS). *Genome Biol.* **9**, R137.
- Zheng, G.X., Terry, J.M., Belgrader, P., Ryvkin, P., Bent, Z.W., Wilson, R., Ziraldo, S.B., Wheeler, T.D., McDermott, G.P., Zhu, J., et al. (2017). Massively parallel digital transcriptional profiling of single cells. *Nat. Commun.* **8**, 14049.
- Zhong, L., Liao, D., Zhang, M., Zeng, C., Li, X., Zhang, R., Ma, H., and Kang, T. (2019). YTHDF2 suppresses cell proliferation and growth via destabilizing the EGFR mRNA in hepatocellular carcinoma. *Cancer Lett.* **442**, 252–261.
- Zhou, J., Wan, J., Gao, X., Zhang, X., Jaffrey, S.R., and Qian, S.B. (2015). Dynamic m(6)A mRNA methylation directs translational control of heat shock response. *Nature* **526**, 591–594.
- Zhou, Y., Zhou, B., Pache, L., Chang, M., Khodabakhshi, A.H., Tanaseichuk, O., Benner, C., and Chanda, S.K. (2019). Metascape provides a biologist-oriented resource for the analysis of systems-level datasets. *Nat. Commun.* **10**, 1523.
- Zhu, X., Huang, S., Zeng, L., Ma, J., Sun, S., Zeng, F., Kong, F., and Cheng, X. (2017). HMOX-1 inhibits TGF- $\beta$ -induced epithelial-mesenchymal transition in the MCF-7 breast cancer cell line. *Int. J. Mol. Med.* **40**, 411–417.
- Zhu, Y., Yan, L., Zhu, W., Song, X., Yang, G., and Wang, S. (2019). MMP2/3 promote the growth and migration of laryngeal squamous cell carcinoma via PI3K/Akt-NF-kappaB-mediated epithelial-mesenchymal transformation. *J. Cell. Physiol.* Published online February 4, 2019. <https://doi.org/10.1002/jcp.28242>.
- Zuber, J., Shi, J., Wang, E., Rappaport, A.R., Herrmann, H., Sison, E.A., Magoon, D., Qi, J., Blatt, K., Wunderlich, M., et al. (2011). RNAi screen identifies Brd4 as a therapeutic target in acute myeloid leukaemia. *Nature* **478**, 524–528.

## STAR★METHODS

### KEY RESOURCES TABLE

REAGENT or RESOURCE	SOURCE	IDENTIFIER
<b>Antibodies</b>		
Rabbit pAb anti-YTHDF2	Proteintech	Cat# 24744-1-AP; RRID: AB_2687435
Rabbit mAb anti-YTHDF2	Abcam	Cat# ab220163; RRID: AB_2868573
Rabbit pAb anti-METTL3	Proteintech	Cat# 15073-1-AP; RRID: AB_2142033
Mouse mAb anti-m6A	Synaptic Systems	Cat# 202 011; RRID: AB_2619890
Rabbit pAb anti-YTHDF2	Aviva Systems Biology	Cat# ARP67917_P050; RRID: AB_2861185
Rabbit pAb anti-Phospho-p44/42 MAPK (Erk1/2)	Cell Signaling	Cat# 4370; RRID: AB_2315112
Rabbit pAb anti-p44/42 MAPK (Erk1/2)	Cell Signaling	Cat# 4695; RRID: AB_390779
Rabbit mAb anti-eif4e	Cell Signaling	Cat# 9742; RRID: AB_823488
Rabbit pAb anti-Phospho-eIF2 $\alpha$ (Ser51) Antibody	Cell Signaling	Cat# 9721; RRID: AB_330951
Rabbit pAb anti-eif2 $\alpha$	Cell Signaling	Cat# 9722; RRID: AB_2230924
Rabbit mAb anti-c-Myc	Cell Signaling	Cat# 13987; RRID: AB_2631168
Mouse mAb anti-GAPDH	Abcam	Cat# ab8245; RRID: AB_2107448
Rabbit mAb anti-BiP	Cell Signaling	Cat# 3177; RRID: AB_2119845
Rabbit mAb anti-Phospho-p38 MAPK	Cell Signaling	Cat# 4511; RRID: AB_2139682
Rabbit mAb anti-p38 MAPK	Cell Signaling	Cat# 8690; RRID: AB_10999090
Rabbit pAb PARP	Cell Signaling	Cat# 9542; RRID: AB_2160739
Rabbit pAb anti-Caspase-3	Cell Signaling	Cat# 9662; RRID: AB_331439
Rabbit mAb anti-Cleaved Caspase-3	Cell Signaling	Cat# 9664; RRID: AB_2070042
Rabbit mAb anti-Phospho-SAPK/JNK	Cell Signaling	Cat# 4668; RRID: AB_823588
Rabbit pAb anti-SAPK/JNK	Cell Signaling	Cat# 9252; RRID: AB_2250373
Rabbit pAb anti-IRE1 $\alpha$	Novus Biologicals	Cat# NB100-2324; RRID: AB_10000972
Rabbit pAb anti-Phospho-IRE1 $\alpha$	Novus Biologicals	Cat# NB100-2323; RRID: AB_10145203
Rabbit mAb anti-Snail	Cell Signaling	Cat# 3879; RRID: AB_2255011
Rabbit mAb anti-ZEB1	Cell Signaling	Cat# 3396; RRID: AB_1904164
Rabbit mAb anti-Vimentin	Cell Signaling	Cat# 5741; RRID: AB_10695459
Rabbit pAb anti-PRSS23	Abcam	Cat# ab201182; RRID: AB_201182
Rabbit pAb anti-DR5	Cell Signaling	Cat# 3696; RRID: AB_10692107
Rabbit mAb anti-Cleaved Caspase-8	Cell Signaling	Cat# 9496; RRID: AB_561381
Rabbit mAb anti-Cleaved Caspase-9	Cell Signaling	Cat# 7237; RRID: AB_10895832
Rabbit mAb anti-BAX	Cell Signaling	Cat# 5023; RRID: AB_10557411
Rabbit pAb anti-RFP	Thermo Fisher	Cat# R10367; RRID: AB_2315269
Rabbit pAb anti-GFP	Abcam	Cat# ab290; RRID: AB_303395
Rabbit mAb anti-HA-Tag	Cell Signaling	Cat# 3724; RRID: AB_1549585
Rabbit pAb anti-Ki67	Abcam	Cat# ab15580; RRID: AB_443209
Rabbit mAb anti-CD31	Cell Signaling	Cat# 77699; RRID: AB_2722705
Mouse mAb anti-puromycin (clone 12D10)	Millipore Sigma	Cat# MABE343; RRID: AB_2566826
Anti-mouse IgG, HRP-linked Antibody	Cell Signaling	Cat# 7076; RRID: AB_330924
Anti-rabbit IgG, HRP-linked Antibody	Cell Signaling	Cat# 7074; RRID: AB_2099233
Goat anti-Rabbit IgG (H+L) Superclonal, Secondary Antibody, Alexa Fluor 488	Invitrogen	Cat# A11034; RRID: AB_2536161
<b>Chemicals, peptides, and recombinant proteins</b>		
Puromycin	ThermoFisher Scientific	Cat# A1113803; CAS: 58-58-2
Poly-D-lysine hydrobromide	Millipore Sigma	Cat# P6407; CAS: 27964-99-4

(Continued on next page)

**Continued**

REAGENT or RESOURCE	SOURCE	IDENTIFIER
(Z)-4-Hydroxytamoxifen	Millipore Sigma	Cat# H7904; CAS: 68047-06-3
Polybrene	Millipore Sigma	Cat# TR-1003-G
Doxycycline hyclate	Millipore Sigma	Cat# D9891; CAS: 24390-14-5
4-Phenylbutyric Acid	Millipore Sigma	Cat# P21005; CAS: 1821-12-1
Tamoxifen	Millipore Sigma	Cat# T5648; CAS: 10540-29-1

**Critical commercial assays**

TruSeq Stranded Total RNA kit	Illumina	Cat# RS-122-2201
Pierce BCA Protein Assay Kit	ThermoFisher Scientific	Cat# 23225
Annexin V: FITC Apoptosis Detection Kit I	BD	Cat# BDB556547
PureLink HiPure Plasmid Filter Maxiprep Kit	Invitrogen	Cat# K2100-17
DNeasy Blood & Tissue Kit	QIAGEN	Cat# 69506
Direct-zol RNA Miniprep Kit	Zymo Research	Cat# R2071
Nextera Index Kit	Illumina	Cat# KAPA#KK4824
KAPA Library Quantification Kit	Illumina	Cat# FC-131-1096
Chromium Single Cell B Chip Kit, 16 rxns	10X Genomics	Cat# PN-1000075
Chromium Single Cell 3' Feature Barcode Library Kit	10X Genomics	Cat# PN-1000079
Chromium i7 Multiplex Kit, 96 rxns	10X Genomics	Cat# PN-120262
Rabbit Specific HRP/DAB (ABC) Detection IHC Kit	Abcam	Cat# ab64261
Hematoxylin and Eosin Stain Kit	Vector Laboratories	Cat# H-3502
Cellular ROS Assay Kit	Abcam	Cat# ab186029
Propidium Iodide Flow Cytometry Kit	Abcam	Cat# ab139418

**Deposited data**

RBP CRISPR screen in MYC-ER HMECs	This paper	GEO: GSE137258
YTHDF2 eCLIP-seq in human breast cancer cell lines	This paper	GEO: GSE137258
m <sup>6</sup> A-seq in human breast cancer cell lines	This paper	GEO: GSE137258
YTHDF2 knockdown RNA-seq in MYC-induced HMECs	This paper	GEO: GSE137258
scRibo-STAMP in MDA-MB-231-LM2 cells with and without YTHDF2 depletion	This paper	GEO: GSE137258
MYC MCF10A ChIP-seq data	ENCODE	ENCSR000DOS
TCF12 MCF-7 ChIP-seq data	ENCODE	ENCSR000BUN

**Experimental models: Cell lines**

Human: Lenti-X 293T	Takara	Cat# 632180
Human: Myc-ER HMECs	<a href="#">Kessler et al., 2012.</a>	Gift from Thomas Westbrook
Human: MDA-MB-231-LM2	<a href="#">Minn et al., 2005</a>	Gift from Thomas Westbrook
Human: MDA-MB-231	ATCC	Cat# HTB-26
Human: MCF-7	ATCC	Cat# HTB-22
Human: SKBR3	ATCC	Cat# HTB-30

**Experimental models: Organisms/strains**

Mouse: Athymic Nude-Foxn1 <sup>nu</sup> 3-4wk, female	Envigo International Holdings, Inc	Cat# 6901
Mouse: Ythdf2 <sup>fl/fl</sup>	<a href="#">Li et al., 2018.</a>	Gift from Chuan He
Mouse: CAG-CreERT mice	Jackson Labs	Cat# 004682
Mouse: CAG-CreERT;Ythdf2 <sup>fl/fl</sup>	This paper	N/A

**Oligonucleotides**

shRNA Library Amplification Primer: Forward: TCGTCGGCAGCGTCAGATGTGTATAAGAGA CAG TAGTGAAGCCACAGAGTA	Integrated DNA Technologies	N/A
--	-----------------------------	-----

(Continued on next page)

### Continued

REAGENT or RESOURCE	SOURCE	IDENTIFIER
shRNA Library Amplification Primer: Reverse: GTCTCGTGGGCTCGGAGATGTGTATAAGA GACAGGGCGCGGAGGCCAGATCTT	Integrated DNA Technologies	N/A
qPCR Primers: See <a href="#">Table S6</a> for primers	Integrated DNA Technologies	N/A
<b>Recombinant DNA</b>		
lentiCRISPR v2	Addgene	Cat# 52961
pINDUCER11 (miR-RUG)	<a href="#">Meerbrey et al., 2011</a>	Gift from Trey Westbrook
TRC lentiviral shRNA vector non-targeting control	Millipore Sigma	SHC002V
TRC lentiviral shRNA vector YTHDF2 (shYTHDF2-1)	Millipore Sigma	TRCN0000168751
TRC lentiviral shRNA vector YTHDF2 (shYTHDF2-2)	Millipore Sigma	TRCN0000167813
TRC lentiviral shRNA vector PRSS23	Millipore Sigma	TRCN0000047042
GIPZ lentiviral shRNA vector YTHDF2	Dharmacon	V2LHS_115143
GIPZ lentiviral shRNA vector YTHDF2	Dharmacon	V2LHS_115142
GIPZ lentiviral shRNA vector YTHDF2	Dharmacon	V3LHS_381614
<b>Software and algorithms</b>		
MaGeCK-v0.5.4	<a href="#">Li et al., 2014</a>	<a href="https://bitbucket.org/liulab/mageck-vispr">https://bitbucket.org/liulab/mageck-vispr</a>
DESeq2-v1.14.0	<a href="#">Love et al., 2014</a>	<a href="https://github.com/mikelove/DESeq2">https://github.com/mikelove/DESeq2</a>
featureCounts-v1.5.3	<a href="#">Liao et al., 2014</a>	<a href="http://subread.sourceforge.net/">http://subread.sourceforge.net/</a>
HOMER-v.4.9.1	<a href="#">Heinz et al., 2010</a>	<a href="http://homer.ucsd.edu/homer/">http://homer.ucsd.edu/homer/</a>
eCLIP-v0.4.0	<a href="#">Van Nostrand et al., 2017</a>	<a href="https://github.com/YeoLab/eclip">https://github.com/YeoLab/eclip</a>
Merge_peaks-v0.0.5	<a href="#">Van Nostrand et al., 2017</a>	<a href="https://github.com/YeoLab/merge_peaks">https://github.com/YeoLab/merge_peaks</a>
MetaPlotR	<a href="#">Olarerin-George and Jaffrey, 2017</a>	<a href="https://github.com/olarerin/metaPlotR">https://github.com/olarerin/metaPlotR</a>
MACS2-v2.1.2	<a href="#">Zhang et al., 2008</a>	<a href="https://pypi.org/project/MACS2/">https://pypi.org/project/MACS2/</a>
SAILOR-v1.1.0	<a href="#">Deffit et al., 2017</a>	<a href="https://github.com/YeoLab/sailor">https://github.com/YeoLab/sailor</a>
Cellranger-v2.0.1	<a href="#">Zheng et al., 2017</a>	<a href="https://github.com/10XGenomics/cellranger">https://github.com/10XGenomics/cellranger</a>
Samtools-v1.3.1	<a href="#">Danecek et al., 2021</a>	<a href="https://htslib.org">htslib.org</a>
Scanpy-v1.4.4	<a href="#">Wolf et al., 2018</a>	<a href="https://github.com/theislab/scanpy">https://github.com/theislab/scanpy</a>

## RESOURCE AVAILABILITY

### Lead contact

Requests for resources and reagents should be directed to and will be fulfilled by the Lead Contact, Gene W. Yeo, Ph.D. ([geneyeo@ucsd.edu](mailto:geneyeo@ucsd.edu)).

### Materials availability

This study did not generate new unique reagents.

### Data and code availability

CRISPR screening, eCLIP, m<sup>6</sup>A-seq, and RNA-seq datasets generated during this study were deposited at GEO and are available under accession number GEO: GSE137258. Source data for dot plots generated from the *in vivo* shRNA screen are provided in [Table S2](#).

## EXPERIMENTAL MODEL AND SUBJECT DETAILS

### Cell lines and cell culture

Immortalized human cell lines were used in this study. HEK293xT (Takara Bio), MDA-MB-231 (ATCC), MDA-MB-231-LM2 (gift from Thomas Westbrook, [Minn et al., 2005](#)), and MCF-7 (ATCC) cells were cultured in DMEM supplemented with 10% fetal bovine serum. SKBR3 (ATCC) cells were cultured in McCoy's 5A Medium supplemented with 10% fetal bovine serum. Cells were passaged every 3 or 4 days with TrypLE EXPRESS (Life Technologies) using standard methods. MYC-ER HMECs (gift from Thomas Westbrook, [Kessler et al., 2012](#)) were cultured in Medium 171 supplemented with MEGS (Life Technologies). Cells were passaged every

3 or 4 days with TrypLE EXPRESS and Defined Trypsin inhibitor. Cells were maintained in a humidified incubator at 37°C with 5% CO<sub>2</sub>. Cells were tested weekly for mycoplasma. Experiments were performed within 5-10 passages after thaw.

### Animal studies

Animal protocols were approved by the Institutional Animal Care and Use Committee at Baylor College of Medicine and at University of California San Diego. Athymic Nude-Foxn1<sup>nu</sup> were purchased from Envigo International Holdings, Inc. CAG-CreERT mice (Jackson labs, stock number 004682) were mated with *Ythdf2*<sup>fl/fl</sup> mice (generous gift from Dr. Chuan He, University of Chicago) (Li et al., 2018) to produce CAG-CreERT;*Ythdf2*<sup>fl/fl</sup> mice. To induce recombination at 8 weeks of age both CAG-CreERT;*Ythdf2*<sup>fl/fl</sup> and *Ythdf2*<sup>fl/fl</sup> littermates were injected with 75mg/kg body weight tamoxifen (Millipore Sigma; T5648) dissolved in corn oil daily for 5 days. Sex, genotype and age information is provided in figure legends and in the methods describing the experiment.

### METHOD DETAILS

#### Lentivirus production and purification

HEK293T cells were seeded on twelve 15 cm plates at 40% confluency the day before transfection. One hour prior to transfection the media was removed and replaced with 8mL of pre-warmed OptiMEM. Transfections were performed using 62.5 μL Lipofectamine 2000, 125 μL Plus reagent, 12.5 μg lentiCRISPR plasmid library, 6.25 μg of pMD.2g, and 9.375 μg psPAX2. Media was changed 6 hours after transfection to DMEM + 10% FBS. After 48 hours, the supernatant was filtered through a 0.45 μm low protein binding membrane. The virus was then ultracentrifuged at 24,000 rpm for 2 hours at 4°C and resuspended overnight at 4°C in PBS. Virus aliquots were stored at -80°C.

#### Multiplicity of infection

For each new cell type, the volume of virus to achieve an MOI of 0.3 was determined by titrating virus in each well (between 5 and 50 μL). 1.5x10<sup>6</sup> cells per well of a 24-well plate were spininfected in medium supplemented with 8 μg/mL polybrene at 2,000 rpm for 2 hours at 37°C. Media (without polybrene) was replaced after the spin and incubated overnight. Cells were split the next morning and half the cells from each condition were treated with puromycin (ThermoFisher Scientific; A1113803). Cells were counted after 3-4 days and MOI was determined by the volume of virus allowing 30% cell survival.

#### MYC-ER HMEC RBP CRISPR screen

For each replicate, 3x10<sup>6</sup> cells were spininfected with RBP CRISPR library (Addgene; #141438) packaged into lentivirus in 5 wells of a 12-well plate in medium supplemented with 8 μg/mL polybrene (Millipore Sigma; TR-1003-G) and spun at 2,000 rpm for 2 hours at 37°C. 2X the amount of virus determined by MOI was added per well. After spininfection, media was replaced (without polybrene) and incubated overnight. The next morning, 5 wells from each replicate were pooled and split onto two 10 cm plates per replicate. Media was replaced containing 2 μg/mL puromycin (ThermoFisher Scientific; A1113803) after 6 hours. Media was changed every 2 days and puromycin was removed after 4 days. 4x10<sup>6</sup> cells were collected and snap frozen in an ethanol, dry-ice bath from each replicate as the day 0 time point. 4x10<sup>6</sup> cells were plated per 15 cm plate for a total of 2 plates per replicate. One plate from each replicate was treated with 15nM 4-Hydroxytamoxifen (4-OHT) (Millipore Sigma; H7904). Cells were cultured for an additional 16 days, changing media and 4-OHT every 2 days, and splitting cells every 4 days, always at a minimum of 4x10<sup>6</sup> cells per 15 cm plate. 4x10<sup>6</sup> cells were harvested on day 8 and day 16 per condition for each replicate and snap frozen.

#### Bulk sgRNA library preparation

DNA libraries were prepared using a targeted-enrichment approach as previously described (Wheeler et al., 2020). Briefly, gDNA was extracted from cell pellets using DNeasy Blood & Tissue kit (QIAGEN; 69506). gDNA samples were sonicated to ~1000bp by Biorupter. sgRNA containing fragments were recovered with biotinylated RNA probes targeting the flanking region on the lenticrispr v2 backbone and pulled down with streptavidin beads. The gDNA fragments were purified and concentrated with DNA Clean and Concentrator-5 kit (Zymo Research; 11-303C). gDNA fragments were PCR'd first with primers flanking the sgRNA

(Forward (5' → 3'): CCTACACGACGCTCTCCGATCTTGTGGAAAGGACGAAACACCG;

Reverse (5' → 3'): GTTCAGACGTGTGCTCTTCCGATCTCCACTTTTCAAGTTGATAACGGACTAGCC); and second with Illumina sequencing adapters. Libraries were analyzed for quality using an Agilent D1000 Screen Tape (Agilent Technologies) and then were sequenced to 6M reads per library on the Hi-Seq4000 in paired-end 55bp mode. Reads were aligned to the RBP library file and candidates were identified using the MaGeCK-v0.5.4 software package (Li et al., 2014).

#### Knockdown experiments

Cells were transduced with TRC lentiviral shRNA vector non-targeting control (NTC; Millipore Sigma; SHC002), and TRC lentiviral shRNA vector YTHDF2 (shYTHDF2-1; Millipore Sigma; TRCN0000168751), (shYTHDF2-2; Millipore Sigma; TRCN0000167813), TRC lentiviral shRNA vector METTL3 (shMETTL3; Millipore Sigma; TRCN0000034717), TRC lentiviral shRNA vector PRSS23

(shPRSS23; TRCN0000047042) or TRC lentiviral shRNA vector TNFRSF10B (shDR5; TRCN0000005929) for 24 hours before treatment with Puromycin (2 mg/mL). Cells were analyzed 6 days after the addition of lentivirus for all assays unless otherwise noted.

### Annexin V/PI apoptosis assay

MYC-ER HMECs were transduced with NTC, shYTHDF2-1, shYTHDF2-2, or shMETTL3 virus at MOI > 1 and selected for 2-3 days with 2  $\mu$ g/mL puromycin (ThermoFisher Scientific; A1113803). MYC expression was induced with 15 nM 4-OHT for 24 hours. The Annexin V apoptosis assay was performed using the Annexin V-FITC kit (BD Biosciences; BDB556547) according to manufacturer's instructions. Cells were analyzed by flow cytometry using the BDLSRFortessa under the FITC (Annexin V) and PerCP-Cy5 (Propidium Iodide) channels with compensation. Analysis and gating were performed using FlowJo.

### Cell cycle analysis

MYC-ER HMECs were transduced with NTC or shYTHDF2-2 virus at MOI > 1 and selected for 2-3 days with 2  $\mu$ g/mL puromycin (ThermoFisher Scientific; A1113803). MYC expression was induced with 15 nM 4-OHT for 72 hours prior to ethanol fixation and propidium iodide staining using the Propidium Iodide Flow Cytometry Kit (Abcam; ab139418) according to manufacturer's instructions. Analysis and gating were performed using FlowJo.

### Pooled *in vivo* shRNA screen and analysis

MDA-MB-231-LM2 breast cancer cells were individually transduced at MOI of 1.2-1.5 with doxycycline-inducible shRNAs (shRNA targeting RNA metabolism genes were cloned from GIPZ plasmid to pINDUCER11 backbone (Meerbrey et al., 2011)):

GIPZ lentiviral shRNA vector YTHDF2 (Dharmacon; V2LHS\_115143), (Dharmacon; V2LHS\_115142), (Dharmacon; V3LHS\_381614)

All cell lines were sequentially pooled in equal ratios. The obtained pool was subcutaneously transplanted ( $3 \times 10^6$  cells per mice) into athymic nude mice (female mice, 4-6 weeks old). Mice were randomized onto and maintained on 5% sucrose water (-Dox) or 5% sucrose water with 2 mg/mL dox (Sigma Aldrich; D9891) (+Dox) 3d post-transplantation. Tumors were measured using calipers and harvested when they reached 1000 mm<sup>3</sup>, approximately 2-3 weeks after engraftment and cells cultured *in vitro* were carried out for 12 population doublings. Genomic DNA from dissected tumors was isolated using the QIAamp DNA mini kit (QIAGEN), and shRNA library was amplified using the following primers (5'-3'):

forward: TCGTCGGCAGCGTCAGATGTGTATAAGAGACAG TAGTGAAGCCACAGAGTA;

reverse: GTCTCGTGGGCTCGGAGATGTGTATAAGAGACAGGGCGCGGAGGCCAGATCTT; The library was indexed using Nextera Index Kit (96 indices) (Illumina; KAPA#KK4824) and purified using PippinHT. The library was quantified using KAPA Library Quantification Kit (Illumina; FC-131-1096) and sequenced at Illumina HiSeq platform ( $\sim 10^6$  reads per tumor with a read coverage of > 10000 reads per shRNA per tumor).

Reads were processed to remove adaptor sequences using Cutadapt (Martin, 2011) and then aligned to the reference library using Bowtie 2 (Langmead and Salzberg, 2012) in end-to-end mode allowing up to a maximum of 3 mismatches/indels compared to the reference sequence. The raw number of reads mapping to each shRNA in each sample was then extracted from the SAM files and DESeq2-v.1.14.0 (Love et al., 2014) was used to determine the normalized abundance of each shRNA in the vehicle and DOX-treated tumors.

### *In vivo* tumorigenicity assays

MDA-MB-231-LM2 breast cancer cells were transduced with validated YTHDF2 targeting pINDUCER11 shRNA 1 (Dharmacon; V2LHS\_115143) and sorted for the top 10% of EGFP-expressing cells on a BD Influx Cell Sorter. Cells were expanded and then subcutaneously transplanted ( $3 \times 10^6$  cells per mouse) into athymic nude mice (female mice, 3-4 weeks old). Mice were randomized onto and maintained on 5% sucrose water (-DOX) or 5% sucrose water with 2 mg/mL dox (Sigma Aldrich; D9891) (+DOX) 14d post-transplantation. Tumors were measured twice, weekly using calipers and harvested when they reached 1000 mm<sup>3</sup> on average and tumors were sectioned and either fixed in 4% paraformaldehyde for IHC analysis or snap frozen and cryopulverized for RNA and protein extraction.

### Immunohistochemistry

Tumor samples were fixed in 4% paraformaldehyde and then paraffin-embedded. Microtome sectioning and hematoxylin/eosin staining was performed by the Moores Cancer Center Histology Core. 5 $\mu$ m thick sections were deparaffinized in Citrisol and rehydrated with graded alcohols. Epitope retrieval was performed by boiling slides for 10 min in sodium citrate buffer (10mM Sodium citrate, 0.05% Tween 20, pH 6.0). DAB staining was performed using Rabbit Specific HRP/DAB (ABC) Detection IHC Kit (Abcam; ab64261) according to manufacturer's instructions. The following antibodies were incubated overnight in 5% goat serum in wash buffer containing 0.025% Triton X-100 in PBS: Rabbit pAb anti-Ki67 (Abcam; ab15580), Rabbit mAb anti-CD31 (Cell Signaling; 77699), Rabbit pAb YTHDF2 (Proteintech; 24744-1-AP), Rabbit pAb anti-RFP (Thermo Fisher; R10367). Hematoxylin (Vector Laboratories; H-3502) was used as a counter stain according to manufacturer's instructions and slides were dehydrated before coverslipping.

### Immunofluorescence

Cells were seeded on poly-D-lysine hydrobromide (PDL) (Millipore Sigma; P6407) coated 8-well chamber slides (Millipore Sigma). Cells were fixed in 4% paraformaldehyde in PBS, permeabilized and blocked 5% normal goat serum, 0.1% Triton-X in PBS for 1 hour at RT. Primary antibody: Rabbit mAb anti-Vimentin (Cell Signaling; 5741), was diluted in blocking buffer and incubated overnight at 4°C. Cells were washed 3 times in 0.1% Triton-X in PBS and incubated with secondary antibody: Goat anti-Rabbit IgG Alexa Fluor 488 (Invitrogen; A32731), for 1 hour at RT, followed by 3 washes and coverslip mounting with Prolong Diamond Antifade Mountant with DAPI (ThermoFisher). Slides were imaged on a ZEISS Axio Vert.A1 inverted microscope.

### eCLIP-seq library preparation and analysis

Experiments were performed as previously described in Van Nostrand et al., 2017 in biological duplicates. Briefly, 20M cells were UV-crosslinked at 400 mJ/cm<sup>2</sup> constant energy, lysed in eCLIP lysis buffer on ice, and sonicated by BioRuptor. Lysate was treated with RNase I to fragment RNA, then protein-RNA complexes were immunoprecipitated (Sheep anti-rabbit Dynabeads) with a YTHDF2 antibody: Rabbit pAb anti-YTHDF2 (Aviva; ARP67917\_P050). Inputs (2% of lysate) were saved and run alongside IP samples. IP samples were stringently washed, and for all samples the RNA was dephosphorylated with FastAP (NEB) and T4 PNK (NEB), followed by on-bead ligation of barcoded RNA adapters to the 3' end (T4 RNA Ligase, NEB). RNA-protein complexes were run on standard protein gels and transferred to nitrocellulose membranes where the RNA in the region 65 kDa – 140kDa was excised off the membrane and proteinase K (NEB) treated. RNA was then reverse transcribed with Superscript III (ThermoFisher) followed by treatment with ExoSAP-IT (Affymetrix) to remove excess oligonucleotides. Samples were cleaned up with Dynabeads MyOne Silane (ThermoFisher) and subject to qPCR to determine the appropriate number of PCR cycles. Libraries were amplified with Q5 PCR mix (NEB), QCed using an Agilent D1000 Screen Tape (Agilent Technologies) and sequenced to 20M reads on the HiSeq4000 in single-end 75 bp mode.

Fastq files were run through eCLIP-v0.4.0 pipeline describe in Van Nostrand et al., 2017. Briefly, adapters and adaptor-dimers were trimmed with cutadapt-v1.14.0, reads were mapped to repeat elements and filtered with STAR-v2.4.0, PCR duplicates were removed with umi\_tools-v0.5.5, and enriched peak regions were called with CLIPPER-v1.2.2v. Peaks were input normalized, reproducible peaks were determined by irreproducible discovery rate ([IDR] [https://github.com/YeoLab/merge\\_peaks](https://github.com/YeoLab/merge_peaks)), and peaks were filtered using merge\_peaks-v0.0.5. Peaks were annotated by gene and region. Motifs were analyzed using HOMER-v.4.9.1 (Heinz et al., 2010). Metagene plots were generated using MetaPlotR-v2.1.2 (Olarerin-George and Jaffrey, 2017).

### m<sup>6</sup>A-seq library preparation and analysis

Experiments were performed as previously described in Dominissini et al., 2013 in biological duplicates. Briefly, 250 μg RNA was extracted using Trizol Reagent (Invitrogen) according to manufacturer's instructions, rRNA depleted (RiboZero), and fragmented to ~100 nt. 1 μg fragmented RNA was saved as input and the rest was immunoprecipitated (Protein G sheep anti-mouse Dynabeads) with an m<sup>6</sup>A antibody: Mouse mAb anti-m6A (Synaptic Systems; 202 011). RNA was precipitated and libraries were prepared with TruSeq Stranded Total RNA Preparation Kit according to manufacturer's instructions. Libraries were QCed using an Agilent D1000 Screen Tape (Agilent Technologies). Libraries were sequenced to ~20M reads on the HiSeq4000 on single-end 75 bp mode. Reads were subjected to cutadapt (Martin, 2011) to remove polyA tracts and adaptor sequences, followed by removal of duplicates and alignment to the human genome build hg19 using the STAR-v2.4.0 (Dobin et al., 2013). Uniquely mapped reads were subjected to peak-calling analysis using MACS2-v2.1.2 software (Zhang et al., 2008) with the following parameters:

```
macs2 callpeak -t IP.sam -c Input.sam -f SAM-gsize = '3137161264' -tsize = 50 -nomodel -extsize = 50 -q 0.1 -down-sample
```

Peaks were filtered based by  $-\log_{10}(q\text{-value}) > 3$  and motifs were analyzed using HOMER-v.4.9.1 (Heinz et al., 2010). Metagene plots were generated using MetaPlotR-v2.1.2 (Olarerin-George and Jaffrey, 2017). Pairwise comparisons to YTHDF2 eCLIP was performed using HOMER-v.4.9.1 (Heinz et al., 2010).

### RNA-seq library preparation and analysis

RNA was extracted with Direct-zol RNA Miniprep kit (Zymo Research; R2071) for two independent non-targeting control biological replicates and two independent shYTHDF2 biological replicates in MYC-ER HMECs induced with 15nM 4-OHT for 48 hours. 1 μg total RNA was rRNA depleted (RiboZero) and processed using the TruSeq Stranded Total RNA Preparation Kit (Illumina; RS-122-2201) according to manufacturer's instructions. Libraries were QCed using an Agilent D1000 Screen Tape (Agilent Technologies). Libraries sequenced to 20M reads on the HiSeq4000 in single-end 75 bp mode.

Adapters were trimmed and reads were mapped to the human genome build hg19 using STAR-v2.4.0. Differential expression was analyzed using DESeq2-v1.22.1 (with significance cutoffs of  $p < 0.001$  and  $\log_2(\text{fold change}) > 1$ , with a minimum TPM of 1 in any sample).

### Western blot

Cells were lysed with cold RIPA buffer (ThermoFisher) with 200X Protease inhibitor and 100X phosphatase inhibitor. Protein was quantified using Peirce BCA Protein Assay Kit. Total protein extracts were run on 4%–12% NuPAGE Bis-Tris gels in NuPAGE MOPS running buffer (ThermoFisher) and transferred to PVDF membranes. Membranes were blocked in 5% nonfat milk in TBST for 1 hour, incubated overnight at 4°C with the following primary antibodies (5% BSA for phospho- antibodies): Rabbit pAb

anti-YTHDF2 (Proteintech; 24744-1-AP), Rabbit mAb anti-YTHDF2 (for mouse tissues, Abcam; ab220163) Rabbit pAb anti-METTL3 (Proteintech; 15073-1-AP), Rabbit pAb anti-Phospho-p44/42 MAPK (Erk1/2) (Cell Signaling; 4370), Rabbit pAb anti-p44/42 MAPK (Erk1/2) (Cell Signaling; 4695), Rabbit Polyclonal anti-Phospho-eIF2 $\alpha$  (Cell, Signaling; 9721). Rabbit mAb anti-eif4e (Cell Signaling; 9742), Rabbit pAb anti-eif2 $\alpha$  (Cell Signaling; 9722), Rabbit mAb anti-c-Myc (Cell Signaling; 13987), Mouse mAb anti-GAPDH (Abcam; ab8245), Rabbit mAb anti-BiP (Cell Signaling; 3177), Rabbit mAb anti-Phospho-p38 MAPK (Cell Signaling; 4511), Rabbit mAb anti-p38 MAPK (Cell Signaling; 8690), Rabbit pAb anti-PARP (Cell Signaling; 9542), Rabbit pAb anti-Caspase-3 (Cell Signaling; 9662), Rabbit mAb anti-Cleaved Caspase-3 (Cell Signaling; 9664), Rabbit mAb anti-Phospho-SAPK/JNK (Cell Signaling; 4668), Rabbit pAb anti-SAPK/JNK (Cell Signaling; 9252), Rabbit pAb anti-IRE1 $\alpha$  (Novus Biologicals; NB100-2324), Rabbit pAb anti-Phospho-IRE1 $\alpha$  (Novus Biologicals; NB100-2323), Rabbit mAb anti-ZEB1 (Cell Signaling; 3396), Rabbit mAb anti-Snail (Cell Signaling; 3879), Rabbit pAb anti-PRSS23 (Abcam; ab201182), Rabbit pAb anti-DR5 (Cell Signaling; 3696), Rabbit mAb anti-Cleaved Caspase-8 (Cell Signaling; 9496), Rabbit mAb anti Cleaved Caspase-9 (Cell Signaling; 7237), Rabbit mAb anti-Bax (Cell Signaling; 5023), Rabbit pAb anti-RFP (Thermo Fisher; R10367), Rabbit pAb anti-GFP (Abcam; ab290), Rabbit mAb anti-HA-Tag (Cell Signaling; 3724), washed 3X for 5 minutes with TBST, incubated for 1 hour at RT in 5% nonfat milk in TBST with secondary HRP-conjugated antibody: Anti-mouse IgG, HRP-link Antibody (Cell Signaling; 7076), Anti-rabbit IgG, HRP-linked Antibody (Cell Signaling; 7074) at 1:5000 dilution, and washed 3X for 5 minutes with TBST. Membranes were developed using Thermo Pierce ECL detection reagents.

### SUnSET assay

MDA-MB-231-LM2 cells expression DOX-inducible YTHDF2-targeting harpin were treated with or without DOX for 3 days. Cells were treated with 10  $\mu$ g/mL for 10 minutes and subsequently processed for western blot analysis as above using the primary antibody, Mouse mAb anti-puromycin (clone 12D10) (Millipore Sigma; MABE343).

### ER stress inhibition assay

MDA-MB-231-LM2 and MDA-MB-231 cells were transduced with NTC, shYTHDF2-1 and shYTHDF2-2, and selected for 2 days with 2  $\mu$ g/mL puromycin (ThermoFisher Scientific; A1113803). shYTHDF2 cells were treated with DMSO only, 1, 2, or 5 mM 4-phenylbutyric acid (4-PBA, Millipore Sigma; P21005) for 72 hours and subsequently processed for western blot analysis as above.

### Cellular ROS assay

MDA-MB-231-LM2 cells were transduced with NTC, shYTHDF2-2, or both shYTHDF2-2 and shPRSS23 virus at MOI > 1 and selected for 2 days with 2  $\mu$ g/mL puromycin (ThermoFisher Scientific; A1113803). The cellular ROS assay was performed (Abcam; ab186029) according to manufacturer's instructions. Cells were analyzed by flow cytometry using the BDSLRFortessa under the APC-Cy7 (deep red) channel. Analysis and gating were performed in FlowJo.

### qRT-PCR analysis

RNA was extracted with Direct-zol RNA Miniprep kit (Zymo Research; R2071) for three biological replicates and cDNA synthesized from 1  $\mu$ g total RNA using High-Capacity cDNA Reverse Transcription kit (Applied Biosystems; 4368814). Real-time PCR was performed using Power SYBR Green PCR Master Mix (Applied Biosystems; 4367659). Values of gene expression were normalized to *GAPDH* expression using the ddCT method. Primer sequences can be found in [Table S6](#).

### Gene Ontology (GO) analysis

GO analyses on single lists were conducted using the GOrilla tool ([Eden et al., 2009](#)) and multiple list analysis were conducted using the Metascape resource ([Zhou et al., 2019](#)). Expressed gene sets with TPM > 1 for each respective cell lines were used as background lists. GO terms were ranked by Bonferroni-corrected hypergeometric p values.

### Time lapse microscopy

Cells were seeded at 5K cells in Incucyte ImageLock plates (Essen BioSciences; 4379). The next day, plates were loaded into the Incucyte<sub>TM</sub> and imaged at 10X magnification for 84 hours every 12 hours. Phase images were analyzed using the Incucyte ZOOM Basic Analyzer to measure confluence.

### TCGA data description

The publicly available dataset from The Cancer Genome Atlas Breast Invasive Carcinoma (TCGA-BRCA) was directly downloaded from the cBioPortal for Cancer Genomics at <https://www.cbioportal.org/>. For detailed information, refer to [Liu et al., 2018](#). For gene expression data, we used mRNA expression z-scores calculated by RNA-Seq by Expectation Maximization (RSEM) and categorized the data by the tumor's clinical subtype. For survival data, we determined the Kaplan-Meier probability using clinical overall survival status by first grouping by high/low *MYC* or *RBP* mRNA expression determined by median z-score (above/below).

We obtained proteomics and phosphoproteomics profiling data from the CPTAC at <https://cptac-data-portal.georgetown.edu/study-summary/S029>. For detailed information, refer to [Mertins et al., 2016](#). After removing the missing values, Pearson's correlation tests were performed to analyze the correlation between each of the known players in the IRE1 $\alpha$  branch of the UPR pathway and YTHDF2 expression for targets found in > 50% of samples.

### scRibo-STAMP assays and analysis

WT MDA-MB-231-LM2 cells or MDA-MB-231-LM2 cells transduced with YTHDF2 targeting pINDUCER11 shRNA 1, sorted for top EGFP expression (Dharmacon; V2LHS\_115143) were each transduced with either RPS2-APOBEC1 or APOBEC1 control STAMP vectors at an MOI < 0.3 to limit copy number variation. Lentivirus was made using pLIX403 Capture-1 control-STAMP-HA-P2A-mRuby or pLIX403 Capture-1 RPS2-STAMP-HA-P2A-mRuby plasmids ([Brannan et al., 2021](#)). Cells were expanded and then subcutaneously transplanted ( $3 \times 10^6$  cells per mouse) into athymic nude mice (female, 10 weeks old). Tumors were allowed to engraft and grow for 6 weeks. Tumors were measured twice, weekly using calipers and mice were given 5% sucrose water with 2 mg/mL dox when tumors were 200 mm<sup>3</sup> on average for 3 days before harvesting. Tumors were washed with sterile PBS and minced with a sterilized blade into 2-3 mm cubes. Tumor pieces were dissociated in enzyme medium ( $\sim 0.1$  cm<sup>3</sup> tumor/ $\sim 2$  mL), shaking for 30 minutes at 37°C. The enzyme medium consisted of 10X enzyme mix (Collagenase IV, 1g/100mL HBSS; (Sigma, #C-5138), Hyaluronidase, 100mg/100mL HBSS; (Sigma, #H-6254), and Deoxyribonuclease, 20,000 U/100 mL HBSS; (Sigma, #D-5025)) in RPMI 1640 medium with 10% Pen/Strep. Cells were strained and spun down. Red blood cells were lysed in water for 20 s and immediately neutralized with PBS +Ca/Mg. Cells were resuspended in media with Pen/Strep and counted with approximately 90% cell viability.

Single cell library preparation and analysis was performed as previously described ([Brannan et al., 2021](#)). Cells were counted and resuspended at a density of 1,000 cell/ $\mu$ L in 0.04% BSA in PBS. Single cells were processed through the Chromium Single Cell Gene Expression Solution using the Chromium Single Cell 3' Gel Bead, Chip, 3' Library v3 (10X Genomics; #PN-1000079, #PN-1000075, #PN-120262) as per the manufacturer's protocol. Sixteen thousand total cells were added to each channel for a target recovery of 10,000 cells. The cells were then partitioned into Gel Beads in Emulsion in the Chromium instrument, where cell lysis and barcoded reverse transcription of RNA occurred, followed by amplification, fragmentation, end-repair, A-tailing and 5' adaptor and sample index attachment as indicated in the manufacturer's protocol for 3' expression capture. Agilent High Sensitivity D5000 ScreenTape Assay (Agilent Technologies) was performed for QC of the libraries and sequenced on an Illumina NovaSeq 6000. Reads were aligned to custom hg19 + lentiviral-genes transcriptomes + TurboRFP. Unique molecular identifier (UMI)-collapsing and sample aggregation were performed using the Cellranger-version 2.0.1 toolkit ([Zheng et al., 2017](#)) provided by 10X Genomics. Analysis of output digital gene expression matrices was performed using the Scanpy-v1.4.4 package ([Wolf et al., 2018](#)). Genes that were not detected in at least five single cells were discarded. Cells with fewer than 1,000 or more than 7,000 expressed genes as well as cells with more than 50,000 unique transcripts or 40% mitochondrial expressed genes were removed from the analysis. Transcripts per cell were normalized to 10,000, added a unit and logarithmized (" $\ln(\text{TPM}+1)$ ") and scaled to unit variance (z-scored). Top 2,000 variable genes were identified with the filter\_genes\_dispersion function, flavor = 'cell\_ranger'. PCA was carried out, and the top 40 principal components were retained. With these principal components, neighborhood graphs were computed with 10 neighbors and standard parameters with the pp.neighbors function. Single-cell scores for comparisons with bulk DEG genes and cell cycle genes were computed with tl.score\_genes and tl.score\_genes\_cell\_cycle functions, respectively.

Single cell edits were called by first computing the MD tag from Cellranger outputs (possorted\_genome\_bam.bam) using Samtools-v1.3.1 calmd ([Danecek et al., 2021](#)) and splitting every read according to their cell barcode. Reads belonging to each cluster of barcodes were combined using a custom script and treated similarly. "Aggregated" edits (across reads that belong to a collection of cells instead of looking at edits per-cell) were used to assess the quality of scRibo-STAMP data, for example when looking at the correlation across regions by combining reads belonging to filtered barcodes into a single BAM file.

Analysis of output digital gene edit matrices was performed using the Scanpy-v1.4.4 package ([Wolf et al., 2018](#)). Matrices for all samples were concatenated and all genes that were not edited in at least 2 single cells were discarded. Cells with fewer than 10 edited genes were removed from the analysis. To calculate the Edits per kilobase of transcript per million mapped reads (EPKM) per gene metric, cumulative edit counts were used (overall 'T' coverage for each edit site called) as determined by SAILOR-v1.1.0 ([Deffitt et al., 2017](#)). Region-specific (either CDS or CDS+3'UTR as defined by hg19 v19 Gencode annotations) edit counts per gene were summed and divided by "per million" mapped read counts that successfully aligned to either CDS or CDS+3UTR, respectively. For analyses, all genes with unique feature mapped counts greater than 0, as defined by Subread featureCounts-v1.5.3 ([Liao et al., 2014](#)), were included. This number was then normalized to the length of either the CDS or CDS+3'UTR of each gene in kilobases (kb) to determine per gene EPKM. EPKM for each cell were normalized to 10,000, added a unit and logarithmized (" $\ln(\text{TPM}+1)$ ") and scaled to unit variance (z-scored). PCA was carried out, and the top 40 principal components were retained. With these principal components, neighborhood graphs were computed with 10 neighbors and standard parameters with the pp.neighbors function. Louvain clusters were computed with the tl.louvain function and standard parameters. Following visual inspection, subsets of Louvain clusters were merged guided by their overlap (or lack thereof) with control-STAMP cells in order to define a Ribo-STAMP-specific clusters. Single cell and mean EPKM per sample heatmaps were generated with the pl.heatmap and pl.matrixplot functions, respectively. Differentially edited genes were determined for each set of Louvain (or modified) clusters with the tl.rank\_gene\_groups function

(method = 'wilcoxon') and up to 100 genes with p value < 0.05 were identified per cluster. Gene ontology was performed using Metascape's multiple gene list function (Zhou et al., 2019) with all edited genes as the background set.

### **QUANTIFICATION AND STATISTICAL ANALYSIS**

Investigators responsible for monitoring and measuring the xenografts of individual tumors were not blinded. Simple randomization was used to allocate animals to experimental groups. All animal studies were performed per institutional and national animal regulations. Power analysis was used to determine the appropriate sample size to detect significant changes in animal survival, which were based on previous survival analyses in our laboratory. All healthy animals with successfully xenografted tumors were included in analyses. All statistical tests are described in figure legends including the test used, exact value of n, definition of center, and precision measures. P values < 0.05 were considered significant and specific p values corresponding to each figure are presented either on the figure itself or in the figure legend.

**Molecular Cell, Volume 81**

**Supplemental information**

**Inhibition of YTHDF2 triggers proteotoxic  
cell death in MYC-driven breast cancer**

**Jaclyn M. Einstein, Mark Perelis, Isaac A. Chaim, Jitendra K. Meena, Julia K. Nussbacher, Alexandra T. Tankka, Brian A. Yee, Heyuan Li, Assael A. Madrigal, Nicholas J. Neill, Archana Shankar, Siddhartha Tyagi, Thomas F. Westbrook, and Gene W. Yeo**

**Figure S1**

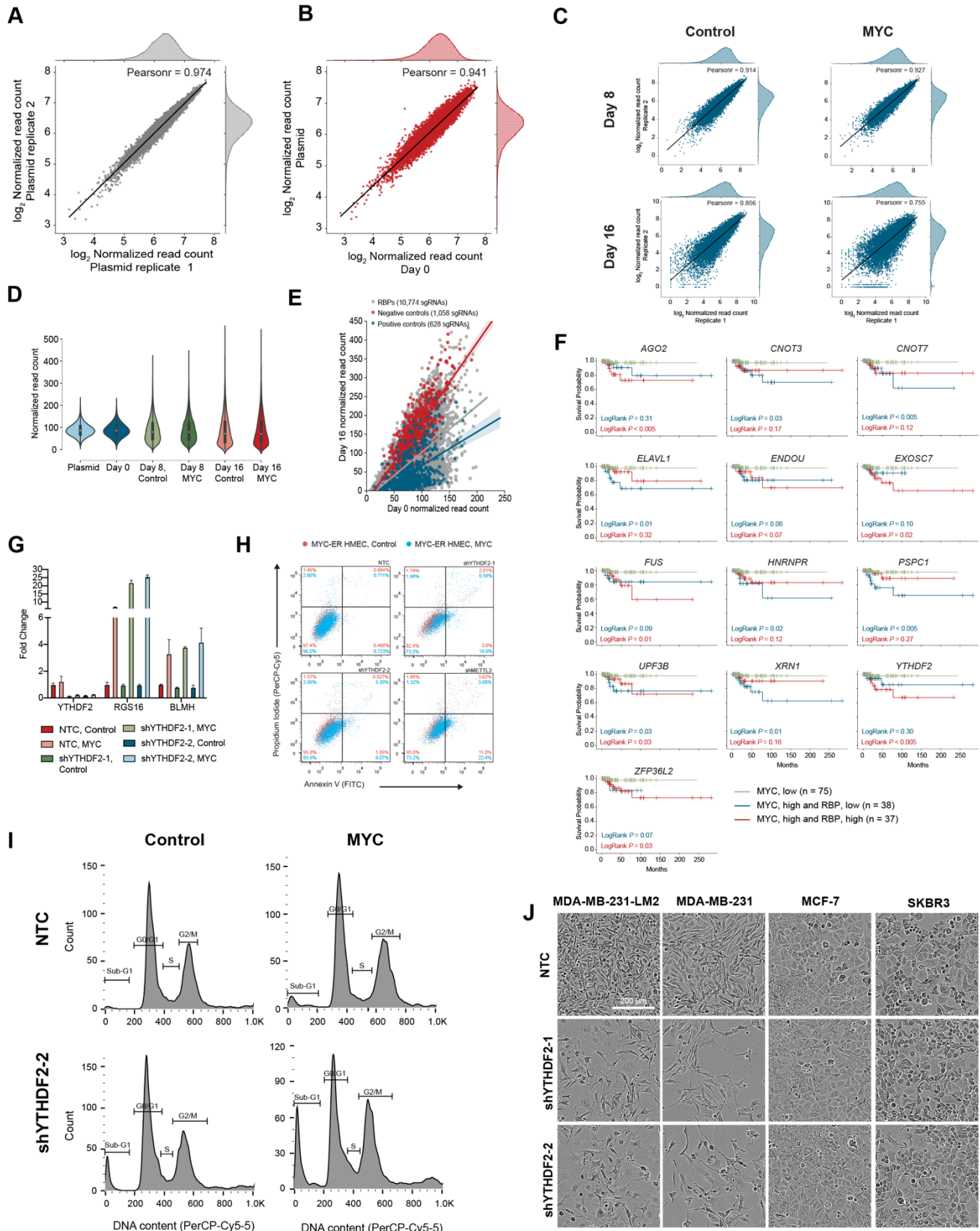


**Figure S1. Efficiency of RBP CRISPR library generation from plasmid to lentiviral particles, Related to Figure 1**

(A) Correlation of normalized read counts between two replicates of plasmid library. R calculated by Pearson's coefficient.

(B) Correlation of normalized read counts between plasmid library and infected cells on day 0. Each condition is representative of two replicates. R calculated by Pearson's coefficient.

(C) Correlation of normalized read counts between replicate samples on day 8 and 16 in both MYC-induced and control conditions. R calculated by Pearson's coefficient.

(D) Violin plot comparing normalized read count distributions in the plasmid library with infected cells on day 0, day 8, and day 16 in MYC-induced and control conditions. Each condition is representative of two replicates.

(E) Scatterplot displaying normalized read counts of infected cells on day 16 compared with day 0. Genes are categorized by negative control (non-targeting), positive control (essential), and RBP. Each condition is representative of two replicates.

(F) Kaplan-Meier survival analysis of basal-like tumors downloaded from TCGA Data Portal (Liu et al., 2018). Curves represent survival probability of tumors with below median (low) *MYC* mRNA expression (green, n = 75), above median (high) *MYC* mRNA expression and low RBP mRNA expression (blue, n = 38), and high *MYC* mRNA expression and high RBP mRNA expression (red, n = 37). LogRank significance compared to tumors with low *MYC* mRNA expression (green).

(G) RT-qPCR analysis relative to *GAPDH* of mRNA extracted from MYC-induced HMECs compared to control with indicated knockdowns. Bars are mean  $\pm$  SD, n = 2 independent replicates.

(H) Flow cytometry analysis of Annexin V/PI staining of MYC-ER HMECs with indicated knockdowns with (blue) and without (red) 24 hours of MYC induction.

(I) Histograms of PI staining by flow cytometry to assess the DNA content of MYC-ER HMECs with and without 3 days of MYC induction for each condition in **Figure 1I**. DNA regions are labeled. Representative of 3 independent replicates.

(J) Representative phase images taken at the endpoint for each condition in **Figure 1J**. Scale bar = 200  $\mu$ m.

**Figure S2**

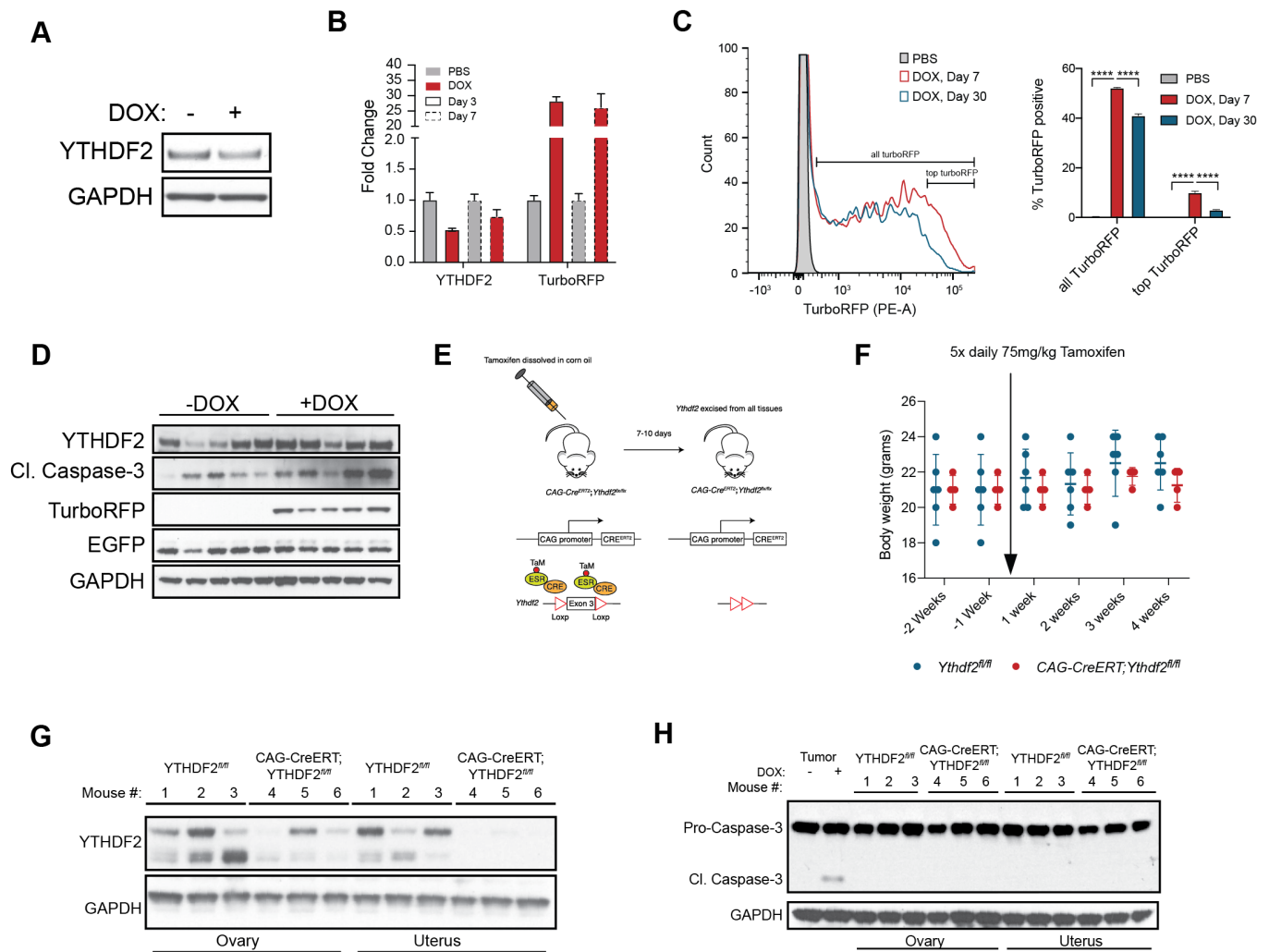


**Figure S2. YTHDF2 depletion is safe and effective *in vivo*, Related to Figure 2.**

(A) Western blot analysis of cell lysates from MDA-MB-231-LM2 cells cultured *in vitro* prior to xenograft injection. Cells were transduced with doxycycline (DOX)-inducible YTHDF2-targeting shRNA and were treated with or without DOX for 7 days before analysis.

(B) RT-qPCR analysis relative to *GAPDH* of mRNA extracted from MDA-MB-231-LM2 cells transduced with DOX-inducible YTHDF2-targeting shRNA after 3 and 7 days of induction *in vitro*. Bars are mean  $\pm$  SD,  $n = 3$  independent replicates.

(C) Flow cytometry histograms of MDA-MB-231-LM2 cells transduced with DOX-inducible YTHDF2-targeting shRNA for TurboRFP expression of cells cultured over time *in vitro*. Bar chart shows gating quantification. \*\*\*\* $p < 0.0001$ , two-way ANOVA test with Dunnett's post-hoc test for multiple comparisons. Bars are mean  $\pm$  SD,  $n = 3$  independent replicates.

(D) Western blot analysis of cell lysates from final tumors, 35 days after DOX induction.

(E) Schematic describing the generation of multi-tissue YTHDF2 knockouts using CAG-CreERT;YTHDF2<sup>fl/fl</sup> mice.

(F) Body weights of male Ythdf2<sup>fl/fl</sup> ( $n = 6$ ) and CAG-CreERT;Ythdf2<sup>fl/fl</sup> ( $n = 4$ ) littermates measured at 6 and 7 weeks and once weekly at weeks 9-12 following tamoxifen administration on week 8.

(G) Western blot analysis of cell lysates from female CAG-CreERT;Ythdf2<sup>fl/fl</sup> ( $n = 3$ ) and Ythdf2<sup>fl/fl</sup> ( $n = 3$ ) littermates from organs taken 10 days following tamoxifen administration.

(H) Western blot analysis of cell lysates from female Ythdf2<sup>fl/fl</sup> ( $n = 3$ ) and CAG-CreERT;Ythdf2<sup>fl/fl</sup> ( $n = 3$ ) littermates from organs taken 10 days following tamoxifen administration run alongside YTHDF2-depleted, DOX-treated and vehicle tumors as controls, to assess for cell death of non-cancerous tissues.

**Figure S3**

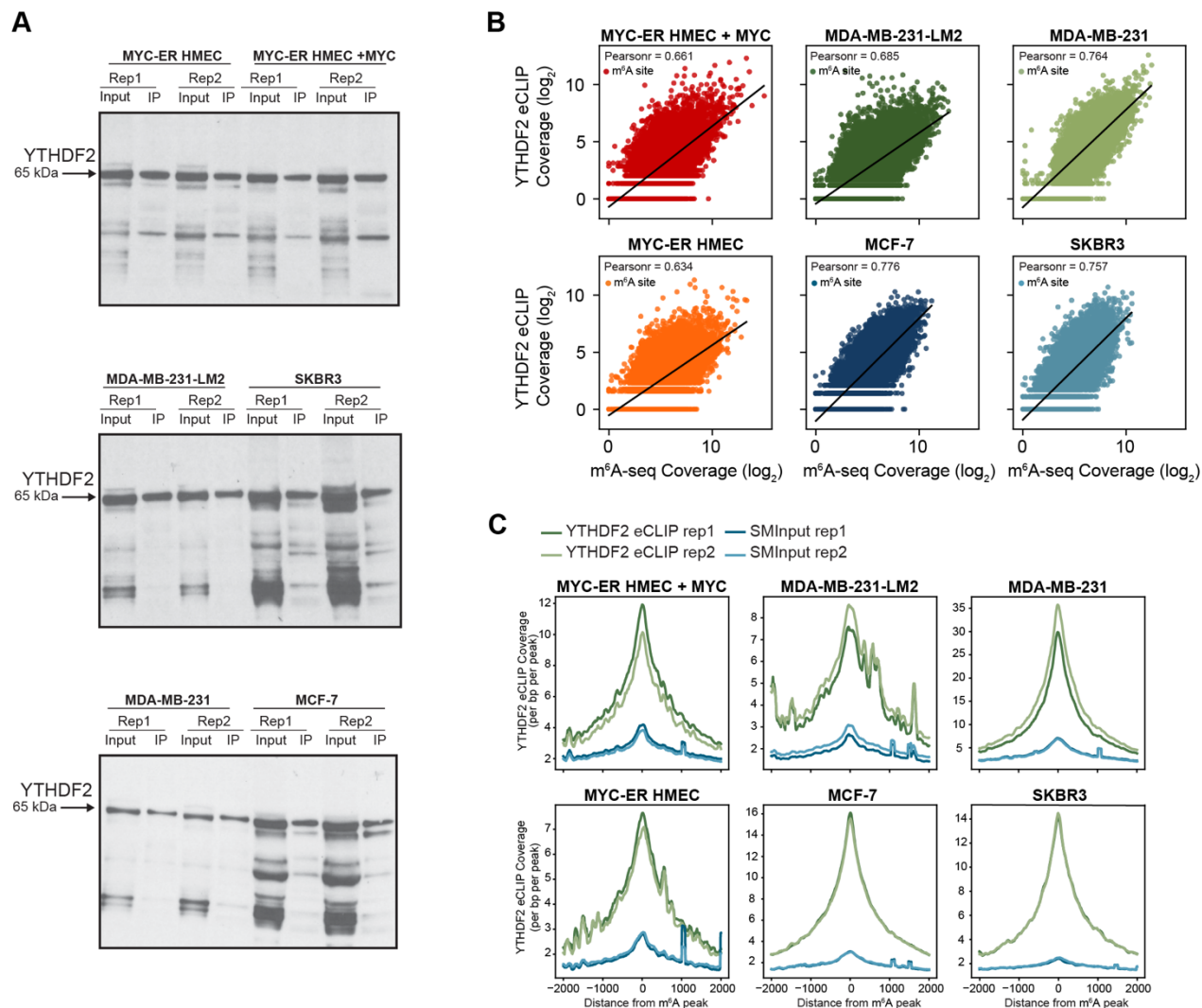


**Figure S3. YTHDF2 eCLIP and m<sup>6</sup>A-seq produce comparable binding profiles in all breast cancer cell lines, Related to Figure 3.**

(A) Immunoprecipitation followed by western blot of YTHDF2 in eCLIP samples.

(B) Correlation between YTHDF2 eCLIP and m<sup>6</sup>A-seq normalized read coverages on m<sup>6</sup>A sites identified by m<sup>6</sup>A-seq. R calculated by Pearson's coefficient.

(C) Histograms displaying the eCLIP sequencing library densities on m<sup>6</sup>A sites identified by m<sup>6</sup>A-seq.

Figure S4

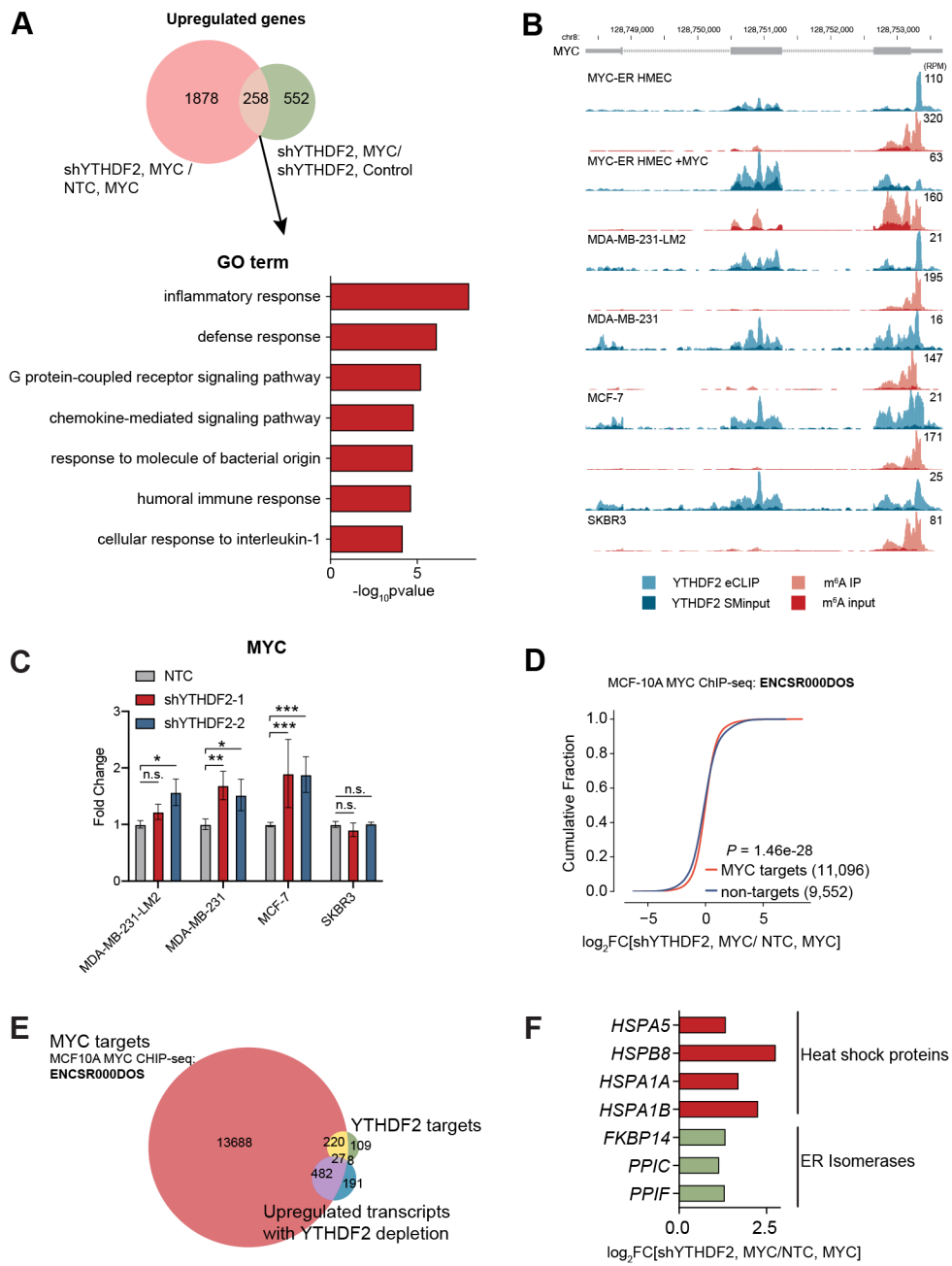


**Figure S4. Stress pathways are upregulated in response to EMT signaling in YTHDF2 depleted, MYC-induced cells, Related to Figure 4.**

(A) Venn diagram comparing differentially upregulated genes in shYTHDF2 MYC-induced HMECS compared to MYC-induced, NTC HMECS or shYTHDF2 control HMECS, respectively ( $p < 0.05$ ) (top). Gene ontology (GO) enrichment of overlapping differentially upregulated genes in Venn diagram (bottom).

(B) Genome browser tracks (hg19) depicting YTHDF2 eCLIP peaks (light blue) over size-matched (SM) input (dark blue) and m<sup>6</sup>A methylation peaks (light red) over input (dark red) on the *MYC* transcript.

(C) RT-qPCR analysis of *MYC* mRNA expression relative to *GAPDH* of mRNA from shYTHDF2 TNBC, HR+ and HER2+ breast cancer cell lines.

(D) Cumulative distribution of the fold change in mRNA expression of shYTHDF2 cells over NTC in MYC-induced HMECs. Describes direct MYC targets (ENCSR000DOS) (red) or non-MYC targets (blue). Two-sided Kolmogorov-Smirnov test compared to non-targets.  $n = 4$  replicates (2 hairpins x 2 biological replicates).

(E) Venn diagram showing the overlap of MYC targets determined in (D) with high confidence YTHDF2 target genes and differentially upregulated genes in shYTHDF2 MYC-induced HMECs.

(F) Bar chart displaying the fold change in mRNA expression of protein folding chaperone genes in shYTHDF2 cells over NTC in MYC-induced HMECs.

**Figure S5**

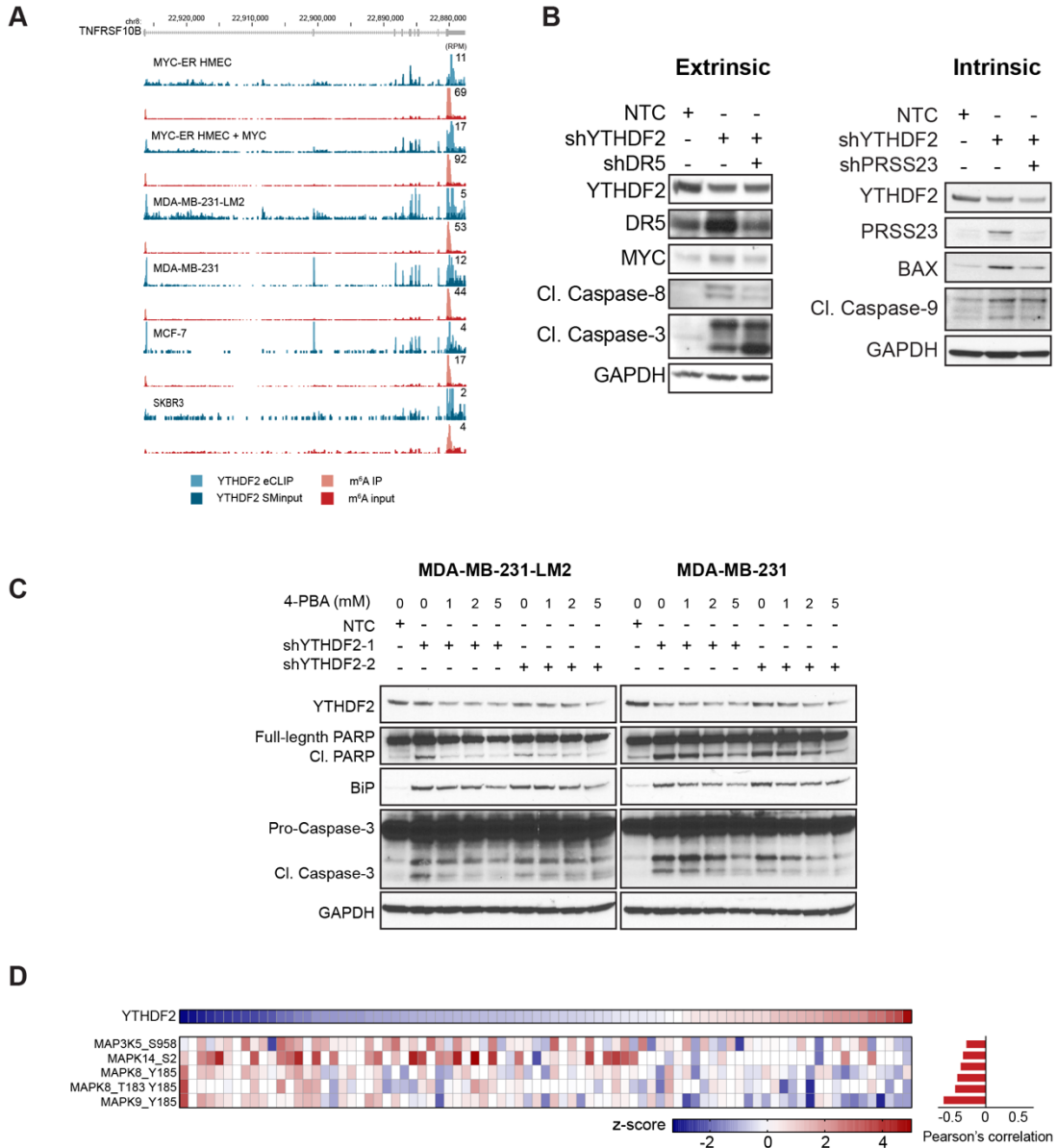


**Figure S5. Inhibition of extrinsic death signaling is insufficient for apoptotic rescue, Related to Figure 5.**

(A) Genome browser tracks (hg19) depicting YTHDF2 eCLIP peaks (light blue) over size-matched (SM)Input (dark blue) and m<sup>6</sup>A methylation peaks (light red) over input (dark red) on the *TNFRSF10B* transcript.

(B) Western blot analysis of cell lysates from shYTHDF2 and YTHDF2/DR5 co-depleted (left) or YTHDF2/PRSS23 co-depleted (right) MDA-MB-231-LM2 cells compared to NTC.

(C) Western blot analysis of cell lysates from NTC or shYTHDF2 TNBC cells cultured with increasing concentrations of 4-phenylbutyric acid (4-PBA).

(D) Heatmap displaying the correlation of protein levels for YTHDF2 and the IRE1 branch of UPR from human breast cancer phospho-proteomics data downloaded from TCGA's CPTAC Data Portal (left) (Mertins et al., 2016). Each column is an individual tumor. Bar plot shows Pearson's correlation scores of YTHDF2 to each phosphorylated protein (right). n = 83 breast cancer tumors. Only significant correlations are shown ( $p \leq 0.05$ ).

**Figure S6**

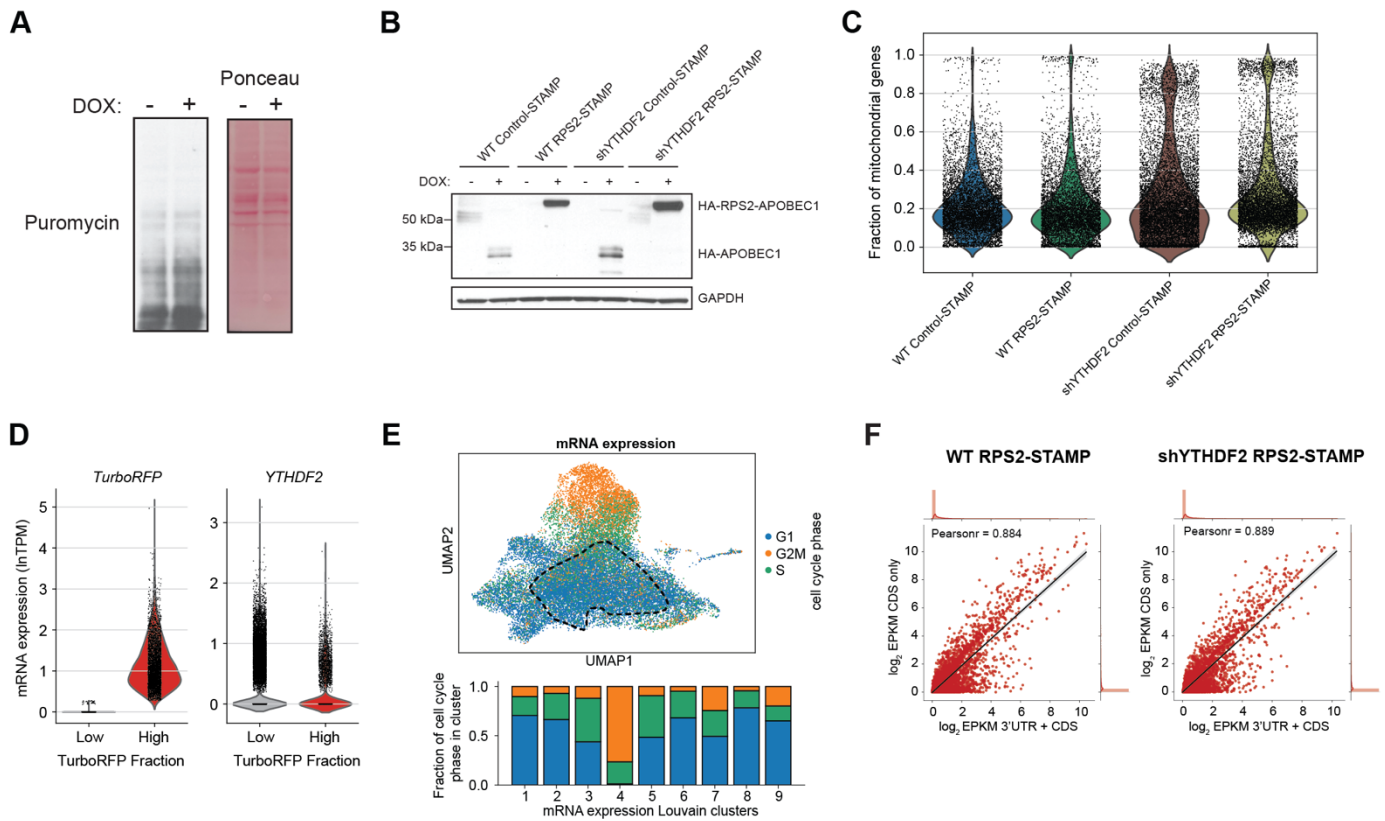


**Figure S6. Single cell analysis of YTHDF2-depleted tumors supports *in vitro* analyses, Related to Figure 6.**

(A) SUNSET western blot analysis of cell lysates from MDA-MB-231-LM2 cells with (+DOX) and without (-DOX) 3 days of YTHDF2 depletion. Cells were treated with 10  $\mu$ g/mL puromycin for 10 minutes. Cell line was generated in **Figures S2A** and **S2B**.

(B) Western blot analysis of cell lysates from control- and RPS2-STAMP cells in wild-type (WT) and shYTHDF2 MDA-MB-231-LM2 cells confirming expression of the HA-tagged fusion proteins following DOX induction.

(C) Violin plots summarizing the fraction of mitochondrial genes detected per cell for control- and RPS2-STAMP single cell experiments for WT and shYTHDF2 conditions.

(D) Violin plots describing TurboRFP and YTHDF2 mRNA expression levels per cell for TurboRFP low- ( $n = 21,464$  cells) or high-expressing ( $n = 3,992$  cells) populations. TurboRFP<sup>High</sup> fraction defined as cells with TurboRFP z-score  $> 0$ .

(E) Uniform Manifold Approximation and Projection (UMAP) analysis of mRNA expression of merged cells from all samples colored by cell cycle phase. Outline indicates the cluster of highest TurboRFP-expressing cells. Bar chart indicates the fraction of cell cycle phase in each mRNA expression Louvain cluster.

(F) Scatterplots correlating normalized, control-STAMP filtered EPKM values counted from aggregated reads in both CDS and 3'UTR regions with EPKM values counted from reads in only CDS regions. R calculated by Pearson's coefficient.

**Figure S7**

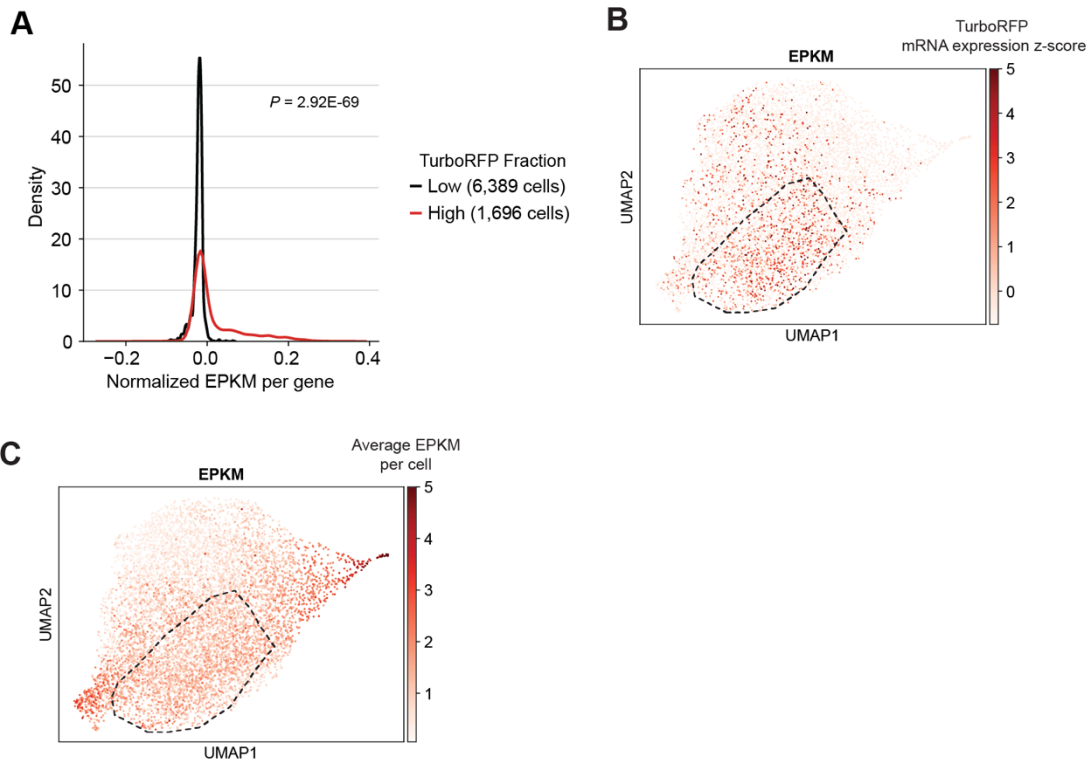


**Figure S7. Single TurboRFP-tagged cells contain edits on more genes per cell on average, Related to Figure 7.**

(A) Distribution of normalized EPKM per gene averaged across all cells in TurboRFP low- and high-expressing populations. TurboRFP<sup>High</sup> fraction defined as cells with TurboRFP z-score > 0. Two-sided Kolmogorov-Smirnov test.

(B) Uniform Manifold Approximation and Projection (UMAP) analysis of control-STAMP filtered EPKM from merged cells in RPS2-STAMP conditions colored by TurboRFP expression. Outline indicates the cluster of highest TurboRFP-expressing cells.

(C) UMAP analysis of Control-STAMP filtered EPKM from merged cells in RPS2-STAMP conditions colored by average EPKM per cell. Outline indicates the cluster of highest TurboRFP-expressing cells.